DESIGN AND EVALUATION OF RECONSTRUCTION METHODS INCORPORATING ESTIMATED MOTION IN GATED CARDIAC EMISSION TOMOGRAPHY

By

JASON G. PARKER

A DISSERTATION PRESENTED TO THE GRADUATE SCHOOL
OF THE UNIVERSITY OF FLORIDA IN PARTIAL FULFILLMENT
OF THE REQUIREMENTS FOR THE DEGREE OF
DOCTOR OF PHILOSOPHY

UNIVERSITY OF FLORIDA

2008

To the sick.

ACKNOWLEDGEMENTS

I thank my Mom and Dad, my sisters Jessica and Julia, and my brother Jimbo, for their love and support. I thank the University of Florida for the rich educational opportunities it has presented me, and the State of Florida for developing a strong and influential institution. I thank Dr. Shukla for his insight and patience throughout many time-consuming experiments in his department. I attribute the majority of my clinical knowledge to the time I spent under his supervision at the Malcolm Randall Veterans Affairs Medical Center in Gainesville, FL. I thank Dr. Hintenlang for his comments and direction on this work, as well as for three years of teaching in the fundamentals of Medical Physics. His broad body of knowledge and expertise plays a key role in the University of Florida Medical Physics program. I thank Dr. Mair for his patient teaching style and encouragement. He has been an invaluable contributor to my education and understanding of the scientific method. It has been an honor work beside him. Finally, I thank my advisor, mentor, and friend, Dr. Gilland. He has treated me fairly and with respect, while insisting on only my best performance. He challenged me in every aspect of my work and in doing so, spurred a wonderful period of intellectual growth for myself.

TABLE OF CONTENTS

page

ACKNOWLEDGEMENTS 4

LIST OF TABLES 7

LIST OF FIGURES 8

ABSTRACT 10

CHAPTER

1 SPECIFIC AIMS 12

2 BACKGROUND AND SIGNIFICANCE 14

Simultaneous Image Reconstruction and Motion Estimation 16
Respiration-Induced Motion Artifacts 17
Channelized Hotelling Observer 19

3 WALL MOTION ESTIMATION FOR GATED CARDIAC EMISSION TOMOGRAPHY: PHYSICAL PHANTOM EVALUATION 21

Introduction 21
Methods 22
Data Acquisition 22
Marker Motion Estimation 24
Myocardium Motion Estimation 24
2-Frame Motion Estimation 27
Motion Estimation Error 27
Summing Estimated Motion Vectors Across Frames 27
Results 28
8-Frame Data 28
2-Frame Data 29
Summing Estimated Motion Vectors Across Frames 29
Summary and Discussion 29

4 IMPROVED RESPIRATORY MOTION CORRECTION IN GATED CARDIAC SPECT 36

Introduction 36
Theory 39
Experimental Methods 41
Algorithms 41
Mathematical Phantom Evaluation 43
Respiratory-Gated Patient SPECT Images 47

Results....48
Motion Estimation on the Noise-Free Phantom Frames....48
Effect of Segmentation....49
Comparison of Methods at Optimal Segmentation....50
Effect of Varying Level of Extra-Myocardial Activity....51
Human SPECT Image....51
Summary and Discussion....52

5 SIMULTANEOUS IMAGE RECONSTRUCTION AND MOTION ESTIMATION IN GATED CARDIAC EMISSION TOMOGRAPHY: A MATHEMATICAL OBSERVER STUDY....60

Introduction....60
Background....61
Motion Compensated Image Reconstruction....61
Simultaneous Image Reconstruction and Motion Estimation....62
Channelized Hotelling Observer....63
Multiple-Array Channelized Hotelling Observer....65
Methods....67
Simulation of Test Data....67
Validation of the CHO....68
Image reconstruction....70
ROC evaluation....71
Direct assessment of SNR using regions-of-interest across the ensemble data....71
Reconstruction without the effects of scatter , attenuation, and detector response....72
Results....72
Validation of the CHO....72
Image Reconstruction....73
ROC Evaluation....74
Direct Assessment of SNR Using Regions-of-Interest across the Ensemble Data....75
Reconstruction without the Effects of Attenuation, Scatter, and Detector Response....75
Summary and Discussion....76

6 CONCLUSIONS....90

APPENDIX

A ROTATION MATRIX AND PARTIAL DERIVATIVES....92

B DETERMINATION OF ROTATION MATRIX....93

C PARTIAL DERIVATIVES USED IN CGQ ALGORITHM....94

REFERENCES....95

BIOGRAPHICAL SKETCH....102

LIST OF TABLES

Table page

3-1 Average estimated motion errors for 8-frame data (pixel units).....35

3-2 Average estimated motion errors for two-frame data (pixel units).....35

3-3 Summed motion errors for OSEM-HS and RM 35

4-1 Relative organ activity concentrations for the simulated NCAT phantom.....59

4-2 Respiratory motion in the mathematical phantom images relative to frame 1. Translations are given in pixels, rotations in degrees. 59

4-3 Motion estimates from the noise-free phantom images.....59

4-4 Average motion estimation errors for the 10 noisy simulated images with background activity at optimal segmentation 59

5-1 Relative organ activity concentrations per pixel for the simulated phantom.....89

5-2 Temporal smoothing kernels.....89

LIST OF FIGURES

Figure page

3-1 Dynamic phantom on imaging bed with close-up of radioactive markers shown on right. Outer shell of phantom is removed. 32

3-2 Projection images obtained from a single angle of the marker acquisition. 32

3-3 Low noise projection images obtained from a single angle of the myocardium acquisition. 32

3-4 Single noise realization obtained after scaling and adding Poisson noise to the projection images in Fig. 3-3. 32

3-5 Reconstructed images obtained from the marker acquisition 33

3-6 Sum-of-Squared Errors vs. Cut-off frequency for 5 (left), 10 (middle), and 50 (right) iterations of OSEM 33

3-7 Transaxial slices of frame 1 of the low noise OSEM, noisy OSEM, and noisy RM reconstructions 33

3-8 Euclidean distance vs. Beta for OSEM-HS (left) and RM (right). 34

3-9 Euclidean distance (ensemble average) vs. frame number for markers 2, 4, 6, and 10. 34

4-1 Select segmentation levels. 54

4-2 Transaxial slice of the segmented human image used for motion estimation. 54

4-3 Select slices of the phantom images at end-diastole. 55

4-4 Horizontal (left) and short (right) axis profiles for Figure 4-3. 55

4-5 Results for average PME found by varying the segmentation parameters. 56

4-6 Reconstructions of the noisy simulated images at end-diastole. 56

4-7 Horizontal (left) and short (right) axis profiles for Fig. 4-6. 57

4-8 Results for average PME found by varying the background activity concentration at optimal segmentation. 57

4-9 Reconstructions of the simulated data at extra-myocardial activity levels of 0.25 and 1.75 (fraction of average). 58

4-10 Reconstructions of the human images with CGQ correction, principal axes correction, and no correction, respectively. 58

5-1 Four frequency bands used in the CHO. 78

5-2 Spatial and frequency domain templates of the four bands used in the CHO. 78

5-3 Phantom source distributions showing the shape and location of the defect. 79

5-4 Noise-free reconstructions for the normal (left) and abnormal (right) datasets. 79

5-5 Regions-of-interest used to calculate SNR directly. 79

5-6 D-prime vs defect contrast. 80

5-7 D-prime vs count level. 80

5-8 D-prime vs number of channels used. 81

5-9 D-prime vs number of training images used. 81

5-10 D-prime vs Butterworth cut-off frequency 82

5-11 Select images used in Figure 5-10. 82

5-12 Results of varying the temporal smoothing kernel number. 83

5-13 Example images of the five levels of temporal smoothing evaluated in Test 6. 83

5-14 Full-width-half-max vs MLEM iteration number on noise-free data. 84

5-15 Full-width-half-max vs Butterworth cut-off frequency on noise-free data. 84

5-16 Full-width-half-max vs temporal convolution kernal on noise-free data. 85

5-17 Example slices of the PS-OSEM and RM reconstructed images. 85

5-18 Motion vector fields for RM reconstructions in Fig. 5-15 86

5-19 Example RM and PS-OSEM images used in the ROC study. 87

5-20 Reciever operating characteristiscs curve for RM and PS-OSEM using 2D CHO on a single lesion. 87

5-21 Reciever operating characteristiscs curve for RM and PS-OSEM using MACHO on a single lesion. 88

5-22 Results of SNR_{ROI} vs. 3D Butterworth cut-off frequency. 88

5-23 Reconstructions of projection data obtained using a simple linear projection operator. 89

Abstract of Dissertation Presented to the Graduate School
of the University of Florida in Partial Fulfillment of the
Requirements for the Degree of Doctor of Philosophy

DESIGN AND EVALUATION OF RECONSTRUCTION METHODS INCORPORATING ESTIMATED MOTION IN GATED CARDIAC EMISSION TOMOGRAPHY

By

Jason G. Parker

December 2008

Chair: David R. Gilland
Major: Nuclear Engineering Sciences

In medical imaging, artifacts due to patient motion can make accurate diagnoses more difficult. The cardiac and respiratory cycles are common sources of patient motion in cardiac emission tomography (ET). For a cyclical motion (such as cardiac or respiratory motion), a gating procedure may be used to freeze the acquisition at the different phases of the cycle, effectively removing the motion blur. However, this reduction in motion blur is at the cost of higher noise levels in the gated images. Our purpose was to develop and test new methods of image reconstruction in cardiac ET that use estimates of patient motion between image frames to improve the noise characteristics of the gated images. The primary method of reconstruction investigated here was one which simultaneously estimates the tomographic images and the frame-to-frame cardiac contraction motion vector fields in a mutually influential manner. The effect this simultaneous approach has on the accuracy of the estimated motion vector fields was tested against a conventional motion estimation method using a physical, dynamic phantom. The simultaneous method was found to have improved motion estimation accuracy compared to the conventional method. Furthermore, a new method for estimating and correcting the respiratory motion of the heart was developed and compared to several other methods proposed in the

literature. The new method shows improved speed, accuracy, and robustness compared to other proposed methods. Finally, the simultaneous reconstruction method was evaluated against a standard reconstruction method in clinical use using a mathematical observer formulated to operate on both single- and multi-frame images, as well as a signal-to-noise ratio measurement using regions-of-interest. In both mathematical observer studies the difference between the simultaneous method and the standard method were not statistically significant. However, the signal-to-noise ratio calculation using regions-of-interest found the simultaneous method to have improved detection characteristics compared to the standard method. Results were found to be significant at the 1% level.

CHAPTER 1
SPECIFIC AIMS

Single photon computed emission tomography (SPECT) myocardial perfusion imaging (MPI) is an important tool in the diagnosis and risk stratification of coronary artery disease. When using the common radiotracer technitium-99m-sestamibi, the 3D images are indicators of myocardial blood flow. The addition of electrocardiographic (ECG) gating during the acquisition procedure allows further analysis of the beating motion of the heart, such as the determination of ejection fraction, wall motion abnormalities, and wall thickening. This motion information, together with the perfusion images, can lead to an assessment of viability in regions of decreased uptake. A negative impact of the gating procedure, however, is that the individual gated images have higher noise levels, impacting both the quality of the images and the accuracy of the motion measurements. The overall goal of this research is to develop and evaluate software methods which improve both the images and motion information in gated SPECT MPI, while maintaining the clinically relevant characteristics of speed, accuracy, and robustness.

In SPECT MPI, there has been considerable research in both image reconstruction and motion estimation; however, the two have rarely been viewed as a single problem. The primary reconstruction method investigated in this work is one which simultaneously estimates the reconstructed image frames and the frame-to-frame non-rigid contraction motion in a mutually influential manner. The impact of this approach on image quality and motion estimation, and ultimately diagnostic accuracy, were investigated.

Specific Aim 1: To test the wall motion estimation accuracy of a simultaneous reconstruction and motion estimation method over the cardiac contraction cycle compared to a conventional motion estimation algorithm.

The hypothesis that a joint reconstruction method is a better method than estimating the images and cardiac contraction motion vector fields separately rests on the assumption that the

motion estimates should improve as the images improve. This hypothesis was tested using point source markers on a physical, dynamic cardiac phantom.

Specific Aim 2: To develop and test a new method for respiratory motion compensation which addresses the clinically relevant issues of speed, accuracy, and robustness.

Motion blur due to the respiratory motion of the heart can blur the myocardial walls and may decrease the diagnostic accuracy of the imaging procedure. In this work we developed an iterative method to correct this motion which treats the heart as a rigid body. The method was tested against other methods in the SPECT literature using both simulated and human data.

Specific Aim 3: To test the detection characteristics of the simultaneous method compared to a standard reconstruction method in clinical use.

The simultaneous method was compared to a standard reconstruction method in clinical use using the channelized Hotelling observer (CHO). The CHO can be thought of as a measure of the signal-to-noise ratio and has been shown to closely model the detection capabilities of human observers.

CHAPTER 2
BACKGROUND AND SIGNIFICANCE

Heart disease is the leading cause of death in the United States [1], and is most commonly characterized by coronary artery disease (CAD). Common initial diagnostic procedures for patients with possible CAD include stress electrocardiography, also known as exercise tolerance testing (ETT), SPECT myocardial perfusion imaging, and stress echocardiography. Analyses of these modalities generally finds the sensitivity and specificity of SPECT MPI and stress echocardiography to be comparable to each other, while both are superior to ETT [2]-[4]. Cost-effectiveness analyses have found SPECT MPI to be a better initial diagnostic tool than ETT or stress echocardiography [5], and this has propelled SPECT MPI to be one of the most important tools in diagnosing patients with heart disease.

Typical SPECT MPI procedure calls for the patient to be injected with a gamma emitting radionuclide, such as thallium-201 or technetium-99m (^{99m}Tc), and subsequently imaged using a rotating gamma camera. ^{99m}Tc is a more favorable radionuclide than thallium-201 in terms of detection, due to the higher energy (140 keV vs. 68-80.3 keV) of the emitted gamma and shorter radiological half-life (6.0 hrs vs. 73.1 hrs). In the case of SPECT MPI with ^{99m}Tc, the sestamibi molecule is attached to the radionuclide, forming the common radiotracer ^{99m}Tc-sestamibi. Shortly after injection of ^{99m}Tc-sestamibi, the radiotracer accumulates within the myocardium in a distribution proportional to blood flow. Unlike thallium-201, ^{99m}Tc-sestamibi crosses cell membranes via passive transport, and thus areas of low uptake generally do not change over time, making ^{99m}Tc-sestamibi a good indicator of blood flow, but less of an indicator of function [6].

An important improvement to SPECT MPI was the introduction of electrocardiographic (ECG) gating [7]. In this procedure, a live ECG signal from the patient is used to bin detected

events into discrete phases of the cardiac contraction cycle. This eliminates much of the motion blur due to the beating motion, but more importantly enables quantitative determination of important functional information regarding the health of the heart, specifically, ejection fraction (EF), regional wall motion abnormalities, and wall thickening. The addition of this functional information has been reported to increase the sensitivity of SPECT MPI to greater than 95% and the specificity as high 94% [2].

A negative impact of ECG gating is that the individual gated images have a decreased SNR, due to the distribution of events over many time frames (typically 8). This decrease in SNR has motivated research into reconstruction methods which take into account the relationship between the images in the time series. In the simplest approach, one may view the time dimension as any other dimension, and the images as a single 4D image. It is then reasonable to perform any number of filter operations across the time dimension that one would use in the spatial dimension (e.g. Gaussian convolution, Fourier filtering). This has the effect of improving the noise characteristics of the images; however, it is at the expense of increased motion blur. Reconstruction followed by spatial and temporal smoothing is referred to as a post-smoothed reconstruction and is a typical approach in the clinical setting due to its simplicity.

In Lalush and Tsui [8] several different distributions were evaluated for use as temporal Gibbs priors in a maximum a posteriori (MAP) reconstruction. The authors found that the different functions and the different weighting schemes they applied controlled the extent to which contrast, noise, and motion blur were present, but that ultimately the choice of these parameters was study specific. It was further shown in Lalush et al. [9] that by including a non-rigid motion estimation in the prior term, the image noise could be improved as in [8], but with a

lower level of motion blur. A fundamental problem with this approach, however, is that the accuracy of the motion estimate suffers from the already high noise levels of the images.

Simultaneous Image Reconstruction and Motion Estimation

A more recent advancement in gated SPECT MPI reconstruction research was the introduction of the simultaneous image reconstruction and motion estimation approach. The simultaneous method rests on two assumptions: 1) a better motion estimate leads to a better reconstructed image, and 2) a better reconstructed image leads to a better motion estimate. The method is implemented iteratively with alternating updates to the reconstructed images and estimation motion vector fields. In Gilland et al. [10] the first use of the simultaneous approach was demonstrated for a simple two-frame system. A conjugate gradient (CG) routine was used to minimize an objective function consisting of three terms: a negative log-likelihood term (reconstruction), an image matching term (motion), and a constraint term on the estimated motion consisting of a biomechanical model of the strain energy of an elastic material undergoing deformation (here representing the myocardium). This paper showed favorable results for the simultaneous method over standard maximum likelihood-expectation maximization (MLEM) [11] reconstructions in a sum-of-squared errors (SSE) sense. The accuracy of the estimated motion vectors was not investigated.

A generalization of the method in [10] was presented in Mair et al. [12]. The method, now referred to as RM (for reconstruction and motion), consisted of two steps: 1) the R-step, in which an image registration objective function was minimized while holding the motion constant, and 2) the M-step, in which the objective function was minimized holding the images constant. The method was generalized to any number of frames, and now had the effect of any one frame being influenced by the frame immediately before and the frame immediately after itself. The accuracy of the reconstructed images was evaluated again in an SSE sense, as well as

qualitatively using visual inspection and profile analysis. The study found that the simultaneous method produced images with better noise properties than those generated with a post-smoothed (PS) ordered subsets-expectation maximization (OSEM) [13] method. The RM-generated motion was evaluated quantitatively using the phantom matching error (PME), a measure of how well the frames matched after deformation by the estimated motion. The authors found that the PME did improve with iteration, confirming the hypothesis that as the images improve the motion estimates improve.

Despite these findings, several problems still remain with RM. The evaluation of the images in Mair et al. [12] does not confirm that the RM generated images are a better diagnostic tool than the current standard, as the SSE does not necessarily reflect the ability of a human to detect lesions. Furthermore, the PME is an indirect measure of motion accuracy and its value is susceptible to noise, image artifacts, and interpolation errors. A direct assessment of the motion accuracy is needed if the RM motion is to be used in a diagnostic environment. Finally, the algorithm is inherently slow. In [12] the authors reported a computational time of 2h 50min (in comparison to a PS-OSEM computational time of ~30s). This is not acceptable for clinical use, and methods for reducing the reconstruction time to < 1min need to be investigated.

Respiration-Induced Motion Artifacts

For imaging modalities requiring scan times longer than a single breath-hold (e.g. SPECT, PET, MR), the motion of the heart due to respiration can introduce blur into the reconstructed images [14]-[16]. Similar to ECG-gating of the cardiac contraction cycle, a gating procedure can be introduced to divide detected events up between phases of the respiratory cycle. If the respiratory motion of the heart between the gated images can be determined, much of the respiration-induced blur can be removed by registering each frame to a reference frame, and summing. Methods for estimating the frame-to-frame respiratory motion of the heart are an

active area of research, with the proposed methods generally falling into one of two categories: external tracking systems, and data analysis methods. A brief review of several common methods is presented here.

External tracking systems use hardware to track patient motion throughout an imaging procedure. One example of this approach was demonstrated in Bruyant et al. [17] in which the authors proposed an external visual tracking system (VTS) to track patient motion during list-mode SPECT acquisition. An elastic sleeve was outfitted with reflective spheres and fit to the patient's chest. The motion of the spheres was tracked throughout the acquisition by five video cameras. After the acquisition, the list-mode data could be adjusted to remove much of the blur due to patient motion. The authors found that the system was highly accurate and robust, and suggested its use for correcting the respiratory motion of the heart in gated SPECT imaging. However, it is known that the motion of markers placed outside the body may not reflect the motion of deeply-embedded structures within the body. Furthermore, external tracking systems may be expensive and require regular quality assurance. Also, currently a VTS cannot be shared between multiple scanners, meaning each scanner in a facility that will use VTS motion correction will require a complete VTS installation.

In contrast, methods for motion correction based on data analysis can be shared by many scanners, do not require maintenance, and are generally less expensive than external tracking systems. Furthermore, data analysis methods have the advantage of measuring the motion of the organ directly. An example of a data analysis method was detailed in Kovalski et al. [18] where the authors proposed modeling the motion of the heart as a rigid body motion during list-mode SPECT acquisition. The respiratory cycle was monitored concurrent to the SPECT acquisition using a piezo-electric chest belt. The data were binned post-reconstruction according to the

respiratory signal and each bin was reconstructed. The motion between the resulting temporal frames was estimated analytically by fitting ellipsoids to the myocardial activity in each frame. This motion was then used to shift each frame back to a reference frame. The resulting images were found to have better spatial resolution than images without correction. However, it was found that often the improvement was small and, from a clinical standpoint, negligible. It is known that the accuracy of data analysis methods can be highly dependant on image noise, myocardial segmentation, and computation time, and the authors suggest that new methods designed to overcome these problems may lead to more significant respiratory motion correction in SPECT MPI.

Channelized Hotelling Observer

In evaluating new reconstruction methods it is perhaps most important to understand how a new method improves (or degrades) lesion detection compared to a standard method. The conventional approach to quantifying imaging system detection performance is by the receiver operating characteristics (ROC) methodology [20]. In ROC analysis, human observers are asked to rate a large number of images based on how sure they are that each image contains a lesion. Their responses are used to generate plots of true positive fraction (TPF) vs. false positive fraction (FPF), often referred to as ROC curves. The area under the ROC curve may be used as an image quality figure of merit. A drawback to ROC analysis is that the studies can be time consuming and often rely on the participation of many observers.

An alternative to performing human ROC studies is to use a mathematical model of lesion detection to evaluate system performance. The Hotelling observer (HO) is one such mathematical model for binary detection tasks which has been shown to correlate well with human observer performance [19]. The HO uses sets of “training” images to develop a co-variance matrix which describes the statistical difference between signal absent (SA) and signal

present (SP) images. After the initial training, the HO can be used to generate a test statistic for a test image which can then be compared to a decision threshold used to classify the current image as SA or SP. Thus, a large number of testing images may be used to mimic a human ROC study.

In Yao and Barrett [21] the HO model was modified with a channel mechanism to imitate the frequency selective "bands" which human observers have been shown to operate under [29]. This extension of the HO, the channelized Hotelling observer (CHO) was found to be a better predictor of human observer performance than the HO. The CHO has been used extensively in the SPECT MPI literature to both optimize system performance and to compare new imaging methods.

CHAPTER 3
WALL MOTION ESTIMATION FOR GATED CARDIAC EMISSION TOMOGRAPHY: PHYSICAL PHANTOM EVALUATION[1]

Introduction

In cardiac emission tomography (ET), improved image quality has been demonstrated when estimated wall motion (non-rigid) is incorporated into 4D reconstruction methods [12], [23]-[24]. One approach is to estimate the motion vector field from an initial filtered backprojection image and use the estimate in the penalty term of a penalized ML approach [24]. Several methods have been proposed for estimating the motion vector fields from reconstructed images, typically using optical flow or elastic deformation models [12], [25]-[29]. In Mair et al. [12] it was shown that simultaneously estimating the reconstructed images and motion vector fields in each iteration resulted in improved image noise.

Since non-rigid motion estimation is playing an important role in cardiac ET reconstruction, methods for evaluating motion estimation accuracy have become important. The objective of this study is to evaluate the accuracy of wall motion estimation methods for gated cardiac ET using a physical, dynamic phantom. This extends our earlier work, which used simulated data of a mathematical phantom with a simple system model that excluded the effects of scatter, detector response, and attenuation. Our approach here is to use high count images of point source markers attached to the myocardial surface of a dynamic thorax phantom to provide an independent measure of the true myocardial motion. As in the earlier work, we compare estimated motion and reconstructed image quality obtained from a simultaneous reconstruction/motion estimation method ("RM" method) [12] with that obtained from a

---

[1] © *IEEE* 2008. Reprinted with permission from (J.G. Parker, D.R. Gilland, "Wall motion estimation for gated cardiac emission tomography: physical phantom evaluation," *IEEE Trans. Nuc. Sci.*, vol. 55, no. 1, pp. 531-536, 2008.).

conventional optical flow method [29] applied to optimized OSEM [30] images. In this work, we will refer to this conventional approach as the "standard" method.

One advantage of the physical phantom, relative to a mathematical phantom, is that the physics of photon propagation and detection are assured to be realistically incorporated into the data. Also, the point marker validation approach enables the accurate tracking of material points on the myocardium. One of the disadvantages of the physical phantom relates to the differences in motion characteristics compared with the typical human heart. For example, unlike the human heart, this phantom myocardium does not exhibit twisting, or wringing, motion, and the base is stationary during contraction [31]. The wall thickening pattern may not match the typical human case. A second disadvantage in this study is that, in order to ensure co-registration with the marker data, no extra-myocardial activity has been included (details in section II). Finally, myocardial defects were not available for this phantom, and their effect on motion estimation could not be studied. It is clear that the significance of this paper rests on the premise that in spite of the shortcomings of the physical phantom, the relative performance of motion estimation methods with this phantom data is equivalent to that with patient data.

Methods

Data Acquisition

A physical dynamic cardiac phantom[2] was modified for motion tracking in this study. The phantom consists of a water-filled torso containing two lungs (each filled with two parts Styrofoam beads and one part water, by volume), a Teflon spine, and a beating heart (Fig. 3-1). The heart assembly is composed of a 50 mL rounded cylindrical latex membrane inserted into an identically shaped 100 mL latex membrane. The volume between the two membranes,

[2] Data Spectrum Corp., Hillsbourough, NC 27278-2300

representing the myocardium, may be filled with radioactive solution to mimic, for example, a myocardial perfusion study with ^{99m}Tc sestamibi. A computer controlled pump is used to expand and contract the volume within the inner membrane while simultaneously sending an ECG signal to the imaging device. Values for stroke volume, ejection fraction, and beats per minute (BPM) can be input to the controlling computer.

The point source marker data acquisition preceded the myocardial activity data acquisition. Ten small point source markers were constructed out of latex tubing and attached to the outer (epicardial) surface of the myocardium with approximately uniform spacing, as shown in Fig. 3-1. A dry syringe was inserted in one end of each marker while another syringe containing ^{99m}Tc was inserted in the other end. The dry syringe was used to apply a negative pressure inside the marker, thus removing any air and ultimately pulling activity out of the opposite, hot syringe. Approximately 3 mCi of ^{99m}Tc was injected into each marker. The volume of ^{99m}Tc solution in each marker was approximately 0.5 mL.

The phantom was programmed for a 50% ejection fraction and 60 BPM. Three consecutive 60 min. gated SPECT scans were acquired on a commercial SPECT system[3] using low energy - high resolution parallel-hole collimators over 120 angles through 360º with 8 gated frames per heart cycle, 3.56 mm pixel size, and 15% energy windows. The three projection sets were then summed. Projection images from a single angle obtained from the marker acquisition are shown in Fig. 3-2.

In order to ensure registration of the marker and myocardial activity images, the phantom was not moved while the markers were allowed to decay to negligible activity levels. Through an access port to the myocardial compartment, ^{99m}Tc solution was injected. Including activity in

[3] Triad 88, Trionix Research Laboratory, Twinsburg, OH 44087

other regions of the phantom would have required moving the phantom, and so this was avoided for this study. A high activity level (73 mCi) and a long scan time (8x60 min.) were used. This high count, low-noise data provided a means of generating an ensemble of datasets at any count level using a Poisson noise generator. Ten noisy datasets were generated such that the count total in a mid-ventricular slice was approximately 215,000. This count level is in a range between gated ^{99m}Tc sestamibi SPECT and ^{18}F-FDG cardiac PET. The ten datasets provided a means of estimating the statistical uncertainty in the results. Low noise, projection images obtained from the myocardial acquisition from a single angle are shown in Fig. 3-3. One of the ten noise realizations is shown in Fig. 3-4.

Marker Motion Estimation

The marker data were reconstructed using 50 iterations of OSEM using 12 projection subsets. Noise in the reconstruction was minimal due to the high-count density of the acquisition; therefore, no spatial smoothing was applied. A 3D ROI was specified for each marker in each frame and the pixel intensity center-of-mass (COM) within each was determined. The vectors describing the motion of the COM's between successive frames were then considered the "true" motion of the myocardium at the location of each marker. Reconstructed images obtained from the marker acquisition are shown in Fig. 3-5.

Myocardium Motion Estimation

The motion of the myocardium was estimated from the noisy projection data of the myocardial activity using two methods: (1) the optical flow method of Horn and Schunck [29] applied to optimized OSEM [30] reconstructions ("OSEM-HS"), and (2) a simultaneous image reconstruction and motion estimation method [12] ("RM").

OSEM-HS Method. In order to ensure high quality images for the OSEM-HS method, the OSEM reconstruction was optimized, in a sum-of-squared errors (SSE) sense, in terms of the

iteration stopping point, 3D spatial filter cut-off frequency, and temporal filter kernel. It should be noted that the parameters which optimize the SSE may not be the best parameters for motion estimation. Values were determined for these parameters that minimized the SSE between the scaled low noise, OSEM reconstruction and a reconstruction of one of the noisy datasets:

$$SSE(\mathbf{f},\hat{\mathbf{f}}) = \sum_{j=1}^{n}\sum_{r}(f_j(\mathbf{r}) - \hat{f}_j(\mathbf{r}))^2 \tag{3-1}$$

where $\mathbf{f} = (f_1, f_2, ..., f_n)$ and $\hat{\mathbf{f}} = (\hat{f}_1, \hat{f}_2, ..., \hat{f}_n)$ are the scaled, low-noise reconstructed image and the noisy reconstructed image, respectively, over *n* frames, and **r** is the 3D voxel index.

To reduce the influence of extra-myocardial noise on the optimization, the index r was confined to pixels in a region of the myocardium. This was achieved using a region-of-interest defined as pixels with intensity above 10% the maximum intensity in the low-noise image. The region defined this way contained all of the myocardium and an approximately one pixel border around the myocardium.

The OSEM reconstruction of the noisy data was tested at stopping iterations of 5, 10, and 50. For each of the three stopping points, a 3D post reconstruction Butterworth filter was applied over a range of cut-off frequency values (0.42-1.7 cycles/cm). Finally, a three-point temporal convolution filter was applied to each of the resulting filtered images with several different weights ({0.1,0.8,0.1} applied once and twice and {0.25,0.5,0.25} applied once). The SSE was computed for each image and the results are shown in Fig. 3-6. The smallest SSE (277.51) occurred using 5 iterations of OSEM with a Butterworth cut-off frequency of 0.91 cycles/cm and a single application of the temporal convolution with weights {0.1,0.8,0.1}. These optimal parameters were then also used to reconstruct the other nine noise realizations.

The motion was estimated by applying the Horn and Schunck optical flow algorithm [29] to the optimized OSEM reconstructions. The Horn and Schunck optical flow algorithm requires a user-defined parameter, β, that weights the contribution of the smoothness constraint. The optimal β was chosen based on the accuracy of the estimated motion (using a Euclidean distance metric described in section II.D below) for a single noise realization, and this optimal β was then used with the other nine noise realizations.

RM Method. The RM method is described in detail in Mair et al. [12]; an overview is presented here. RM is a method for simultaneous reconstruction and motion estimation that alternates between pixel intensity updates (R-step) and motion updates (M-step).

The R-step is a penalized likelihood method that incorporates the estimated motion into the penalty term. The M-step employs sequential quadratic programming and the conjugate gradient algorithm to compute motion given the current image estimate. The M-step used the simpler smoothness constraint of Horn and Schunck [29] rather than the strain energy constraint in Mair et al. [12]. For this study, 50 RM iterations were used where each RM iteration comprised 2 R-step iterations and 1 M-step iteration.

Two user-defined parameters, α and β, are used in RM. Parameter α is the scalar for the likelihood function and was chosen empirically for this study. Parameter β weights the contribution of the smoothness constraint as in the HS method, and was chosen by the same method used in the OSEM-HS method.

The RM reconstructions were filtered with a Butterworth filter with cutoff frequency equal to 1.5 cycles/cm. Example transaxial slice images of low noise OSEM, noisy OSEM, and noisy RM are shown in Fig. 3-7.

2-Frame Motion Estimation

To further evaluate the motion estimation methods at higher magnitudes of motion, 2-frame datasets containing only the end-diastolic (ED) and end-systolic (ES) frames (corresponding to frames 8 and 3, respectively) from each noise realization were created. Optimal reconstruction and motion estimation parameters were determined using the same methods employed with the 8-frame data.

Motion Estimation Error

The accuracy of the estimated motion vector fields was determined by calculating the Euclidean distance (i.e. the magnitude of the vector difference) between the estimated and the marker-based, true motion vector in the vicinity of each marker. In computing this error metric, the estimated motion was the average motion over the eight voxels nearest the marker center-of-mass.

The motion error was calculated for each marker in each frame and in each noise realization, for both the 8-frame and 2-frame datasets. The mean error and standard deviation (σ) over the 10 realizations was computed at each marker location.

Summing Estimated Motion Vectors Across Frames

The estimated motion vectors at each marker location were added across several systolic frame-to-frame intervals (8→2, 8→3) and compared to the net movement of the markers through corresponding frame intervals. The purpose for this analysis was two-fold: (1) to determine whether the motion errors accumulate over frames or if one or both of the angle and magnitude components of the errors cancel across frames and, (2) to compare the accuracy of the total systolic motion estimation using either a series of small frame intervals or a single large frame interval. This frame-to-frame vector summing involved 3D linear interpolation of the estimated motion vectors in the vicinity of the markers at each frame.

Results

8-Frame Data

The results of the optimal β search for OSEM-HS and RM for the 8-frame data are shown in Fig. 3-8. The figure shows the motion error as a function of β averaged across all markers and all frames for a single noise realization. The optimal β was 0.15 for both OSEM-HS and RM.

This value of β, when applied to the ensemble data, resulted in an average motion error (including all markers and all frames) of 0.15 pixels ($\sigma = 0.001$) for OSEM-HS and 0.13 pixels ($\sigma = 0.001$) for RM. A more detailed presentation of these results is given in Fig. 3-9, which shows plots of the frame-by-frame, ensemble average motion error for four selected markers. The plots emphasize the relationship between motion magnitude and estimated motion error (i.e. an increase in motion magnitude yields an increase in estimated motion error). Frames 1 and 4 are the frames of peak systolic and diastolic motion, respectively, and thus, the motion error is often greatest in these frames. The errors were similar for both methods except frame 1, the frame of greatest motion magnitude, where the RM error was significantly smaller for 7 out of 10 markers.

Table 3-1 summarizes the motion errors (ensemble average) at each frame by averaging across all markers. Also included is the true magnitude for each frame, again to emphasize the relationship between motion magnitude and motion estimation error.

The significance of the differences in the estimated motion error between the two methods was evaluated in each frame based on paired t-tests using the average marker error for each noise realization. The differences were significant at the 5% level for all but frame 7. In spite of the statistical significance of the differences, the practical significance is questionable given the generally small magnitude of the differences.

2-Frame Data

The optimal β for the 2-frame data was found to be 0.06 for OSEM-HS and 0.03 for RM. These values of β applied to the ensemble data resulted in an average motion error including all markers and all frames of 0.55 pixels ($\sigma = 0.005$) for OSEM-HS and 0.37 pixels ($\sigma = 0.004$) for RM. Table 3-2 gives the frame-by-frame motion error and true motion magnitude averaged across all markers.

The differences between methods for both frames were found to be statistically significant at the 5% level. For this 2-frame data, which has greater frame-to-frame motion magnitude than the 8-frame data, the better performance of RM was more pronounced. The practical significance of this difference requires further investigation.

Summing Estimated Motion Vectors Across Frames

The summed estimated motion errors (averaged over all ten markers over all ten noise realizations) for both OSEM-HS and RM are given in Table 3-3. Since the angle error decreases as the motion vectors are summed over frames, whereas the magnitude error increases, these limited observations suggest that the angle error cancels over frames, and the magnitude error accrues over frames. The summed motion for the complete systolic range (Table 3-3, row 2) is only slightly worse than the motion obtained by estimating the motion directly between the two frames (Table 3-2, row 1). Further investigation is needed to determine if there are situations in which the method of summing over smaller intervals could produce improved accuracy over direct estimation of motion between two frames.

Summary and Discussion

This paper describes a study that used a physical phantom with point source markers to evaluate the accuracy of wall motion estimation for gated cardiac ET. Of the two estimation methods that were evaluated—the established optical flow method of Horn and Schunck and a

simultaneous reconstruction and motion estimation method—the simultaneous method resulted in a statistically significant lower overall error, and the difference was greatest for the largest true motion magnitude. The absolute difference between the methods overall was relatively small, and it is reasonable to question the practical significance of the difference if the methods were to be used, for example, within a motion-compensated reconstruction algorithm. Aside from assessing the relative performance of these particular motion estimation methods, a more general contribution of this work has been the development of a physical phantom-based method for evaluating motion estimation methods.

Several limitations of this study should be noted, and the first concerns the regions of the myocardium that were sampled for this study. The 10 point markers do not sample the entirety of the myocardium, and so the regional variation may have been missed. More specifically, the markers were located only on the epicardial, or outer, surface of the phantom myocardium. It is known that the motion magnitude on this surface is less than that on the endocardial, or inner, surface, and it is reasonable to question if the results would be the same for the more challenging endocardial region. Results from this study suggest that the relative advantage of the simultaneous method increases as the true motion magnitude increases. Finally, the markers could not be located within the myocardium (i.e. away from either surface), which would be expected to be more challenging than the high image contrast regions located along the surfaces.

Another limitation of this study concerns the differences in motion characteristics of the phantom compared with the typical human heart. One prominent difference is the degree to which the true motion is tangential to the myocardial surface. In human hearts, this component is substantial and coincides with the wringing motion that has been observed [31]; in the phantom,

this component is relatively small. It is known that a weakness of the motion estimation methods tested here is their ability to estimate this tangential component of motion.

The results of this physical phantom study are generally consistent with an earlier study that used a mathematical phantom [12]. Specifically, both studies demonstrated more accurate motion estimation with the simultaneous RM method compared with an independent motion estimation method applied to fixed, reconstructed images. In the earlier work, the independent estimation method was the M-step of the RM method applied to optimized OSEM images. The earlier work also demonstrated improved image quality with RM compared with OSEM; however, the study here showed only minor differences in image quality with the two reconstruction methods. In terms of α and β, different values were found appropriate for this data compared with the mathematical phantom data. For β, this difference is due to the different smoothness constraints used in the two studies. For α, this difference is due to the extra-myocardial (i.e. liver) activity included in the mathematical phantom, which greatly affects the likelihood function value, and, therefore, the choice of α.

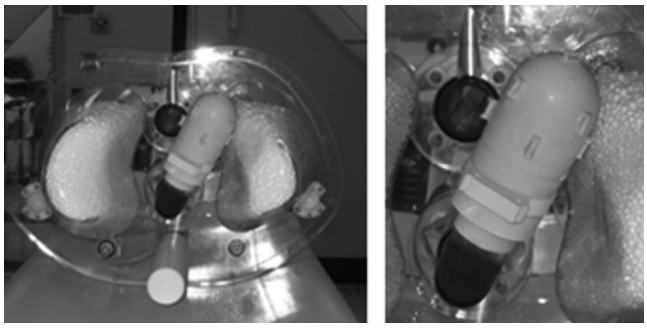

Figure 3-1. DCP on imaging bed with close-up of radioactive markers shown on right. Outer shell of phantom is removed.

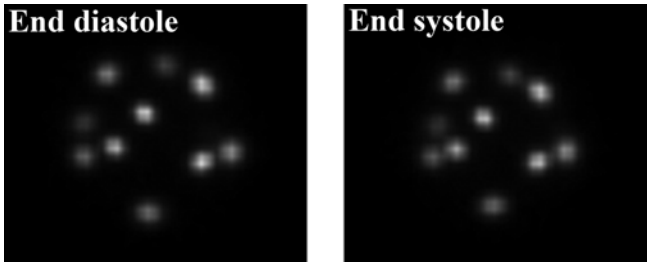

Figure 3-2. Projection images obtained from a single angle of the marker acquisition.

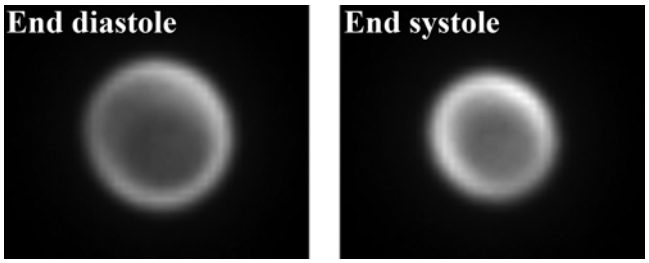

Figure 3-3. Low noise projection images obtained from a single angle of the myocardium acquisition.

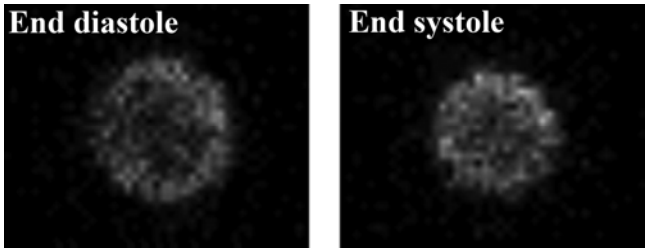

Figure 3-4. Single noise realization obtained after scaling and adding Poisson noise to the projection images in Fig. 3-3.

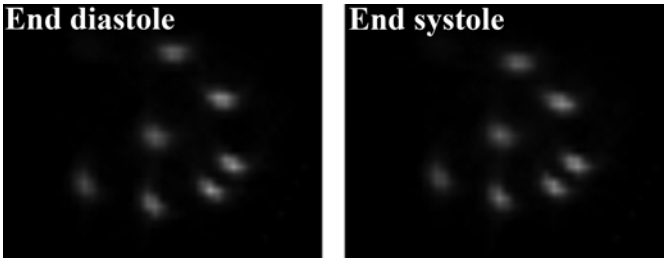

Figure 3-5. Reconstructed images obtained from the marker acquisition, shown with slices 14-34 summed.

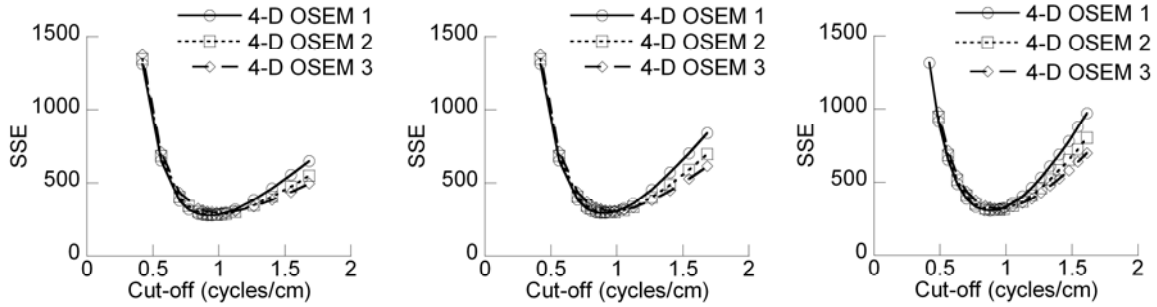

Figure 3-6. SSE vs. Cut-off frequency for 5 (left), 10 (middle), and 50 (right) iterations of OSEM, where 4-D OSEM 1 = single application of {0.1,0.8,0.1} temporal filter, 4-D OSEM 2 = two applications of {0.1,0.8,0.1} temporal filter, and 4-D OSEM 3 = single application of {0.25,0.5,0.25} temporal filter.

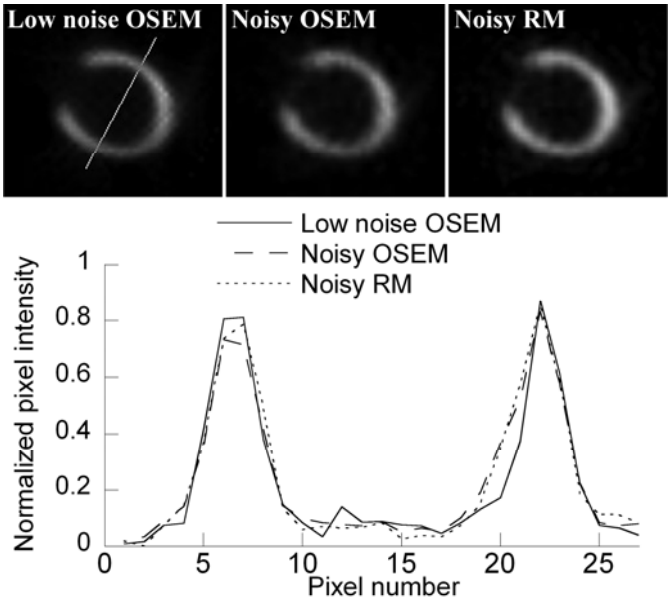

Figure 3-7. Transaxial slices of frame 1 of the low noise OSEM, noisy OSEM, and noisy RM reconstructions. Profiles for the oblique line shown in the low noise image are normalized and shown in the plot.

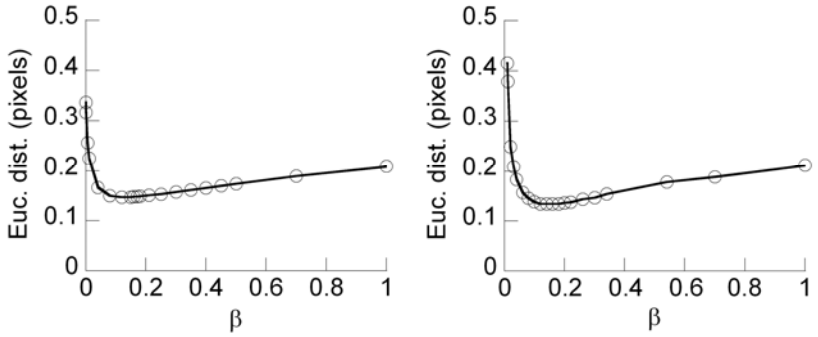

Figure 3-8. Euclidean distance vs. Beta for OSEM-HS (left) and RM (right).

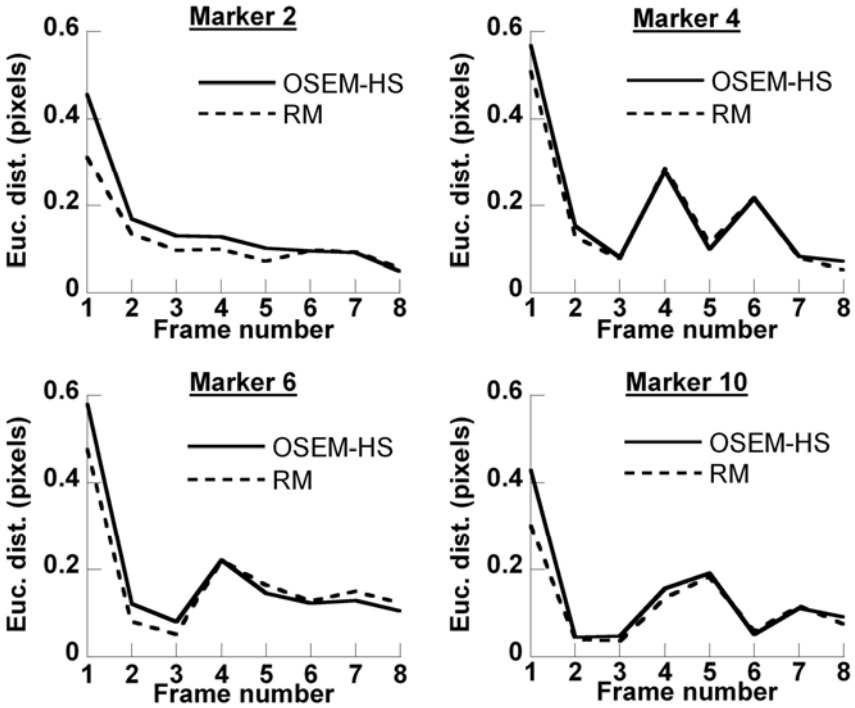

Figure 3-9. Euclidean distance (ensemble average) vs. frame number for markers 2, 4, 6, and 10. The plots emphasize the relationship between motion magnitude (greatest in frames 1 and 4) and estimated motion error.

Table 3-1. Average estimated motion errors for 8-frame data (pixel units)

Frame number	True magnitude	OSEM-HS Error	RM Error
1	0.939	0.429	0.328
2	0.286	0.100	0.087
3	0.217	0.077	0.069
4	0.463	0.150	0.141
5	0.307	0.119	0.116
6	0.194	0.102	0.101
7	0.211	0.110	0.105
8	0.166	0.098	0.100

Table 3-2. Average estimated motion errors for two-frame data (pixel units)

Frame number	True mag.	OSEM-HS Error	RM Error
1 (ED → ES)	1.347	0.462	0.351
2 (ES → ED)	1.347	0.642	0.386

Table 3-3. Summed motion errors for OSEM-HS and RM

	OSEM-HS			RM		
Frame interval	Motion error (pixels)	Angle error (degrees)	Mag. error (pixels)	Motion error (pixels)	Angle error (degrees)	Mag. error (pixels)
8 → 2	0.441	17.6	-0.368	0.347	15.6	-0.252
8 → 3	0.487	14.5	-0.401	0.386	13.0	-0.288

CHAPTER 4
IMPROVED RESPIRATORY MOTION CORRECTION IN GATED CARDIAC SPECT

Introduction

In cardiac imaging modalities requiring scan times longer than a single breath-hold (e.g. PET, SPECT, MR), the motion of the heart due to respiration introduces blur into the tomographic images [14]-[16], [33]-[34]. By sensing the phase of the respiratory cycle, a gating procedure may be used to produce a time series of images with reduced motion blur. When combined with electrocardiographic (ECG) gating of the cardiac contraction cycle, the acquisition is referred to as a dual-gated study [35]-[36] and produces a matrix of projection sets. A drawback to respiratory-gating, similar to ECG-gating, is higher noise levels in the gated images [37]-[38]. To combat the increased noise levels of respiratory-gated images in emission tomography, motion correction using an estimate of the heart motion between the image frames combined with temporal summing, has been proposed [17]-[18],[36],[39]-[46].

Gating of the respiratory cycle may be accomplished by affixing a piezo-electric elasticized belt around the patient's chest. As the patient breathes, a signal is generated corresponding to the tension in the belt. The signal may be input to the imaging device as a representation of the respiratory cycle, similar to ECG-gating of the cardiac contraction cycle. Image data may be binned in terms of respiratory amplitude or phase, where amplitude binning has less in-frame motion blur than phase binning, but phase binning has better noise level uniformity across bins [47].

Given the gated image frames, many techniques currently exist for estimating respiration-induced heart motion. Physical devices have been used that track the motion of markers placed on the patient's chest throughout the acquisition [17],[39]-[40]. These devices offer high precision; however, the motion of deeply-embedded structures within the body may be different

than that of the surface of the body. Furthermore, implementation of physical tracking methods requires hardware integration and calibration for each scanner in a facility, which may be expensive and require regular quality assurance.

Motion estimation methods based on image data analysis alone are easier to implement and have the advantage of estimating the motion of the organ directly. Rigid-body [18],[41]-[43], affine [44],[45], and deformable models [16],[36] of the respiratory heart motion have all been shown to successfully decrease respiration-induced artifacts in cardiac imaging. In SPECT, the rigid-body model of the heart [48] has been used widely due to spatial resolution constraints, which place an upper-bound on the extent of the improvement possible using motion estimation and temporal summing. A drawback of image data analysis methods is that their accuracy is highly influenced by image noise, reconstruction artifacts, and available computational resources.

Within the data analysis approach, both analytical and iterative methods have been investigated in estimating the respiratory heart motion from tomographic data. Analytical methods [18],[41]-[43] are generally faster than iterative methods [44]-[46], but their accuracy may be highly dependent on the level of noise in the images. Iterative methods, aside from their high computational costs, often require a good initial estimate to reach convergence [49]. In Klein et al. [44], the affine motion for a given frame-pair used an initial estimate defined as the motion estimate from the immediately preceding frame-pair. A cost function was implemented which penalized deviations from this starting estimate. The method showed convergence, but required a user-defined weighting parameter on the cost function, which may complicate the use of the method in a clinical environment. Furthermore, the authors reported an average computation time of 720s. The method in Dey et al. [45] used spatio-temporal penalty terms

which penalized deviations from the simple-harmonic oscillation equation. The method demonstrated convergence but again required user-defined weighting parameters on the penalty term.

We previously investigated methods for estimating and correcting the respiratory motion of the heart iteratively without user-defined parameters or penalty terms [46]. The method used a rigid-body model with rotation parameterized by Euler angles and iteratively minimized an image-registration function using an optimized conjugate gradient method. The Euler angles correspond to a rotation about the x-axis followed by a rotation about the y-axis, followed by a second rotation about the x-axis. In Parker et al. [46], the motion was estimated after summing the ECG-gated frames. This summing adds motion blur to the images, but increases the SNR. The method was slow due to repeated calculation of the objective function and its derivatives which required extensive trigonometric evaluations. On modern computer architectures, trigonometric functions are approximated using simple iterative equations [50], and thus may be ill-suited for use in deeply-embedded loops.

To improve the computational efficiency of the method in [46] while maintaining high accuracy and convergence, here we investigate the use of the quaternion parameterization of rotation [51] in iteratively estimating the rigid body respiratory motion of the heart. Quaternions have been used extensively in computer animation and gaming industries due to their simplicity and improved physical characteristics [52] compared to Euler representations. For example, gimbal lock, a condition resulting when the second Euler angle is equal to 90° and a degree of freedom is lost, is avoided using the quaternion representation. Furthermore, a quaternion-parameterized rotation matrix is free of trigonometric functions, and we hypothesize that this simplification will reduce the computational burden of repeated calculations of the objective

function and its partial derivatives. We compare this method quantitatively in terms of speed, accuracy, and robustness to several other iterative and analytical techniques, using simulated data of a mathematical phantom. The quaternion method is further evaluated on a respiratory phase binned human SPECT image in terms of computation time and image quality after correction by the estimated motion. It is shown that the use of the quaternion representation enables a fast, accurate, and robust model for respiratory motion correction, which has practical applications not only in SPECT but also in other imaging modalities in which breath-hold acquisition is impractical, such as PET and MR.

Theory

We represent the image space by a discrete space variable $\mathbf{r} = (x,y,z)$, and assume a series of tomographic image frames $f_1, f_2, \ldots, f_J$. We assume that the frame-to-frame motion of an object can be modeled as a rigid body. We consider the problem then of forming a single composite image by registering and summing all frames to the "reference frame", f_1, using an estimate of the rigid-body motion between each frame and the reference frame.

The rigid body motion between f_1 and f_j is estimated by minimizing the image registration objective function:

$$E_j\left(\mathrm{Q},\mathbf{b}\right) = \sum_{\mathbf{r}} \left(f_1\left(\mathbf{r}\right) - f_j\left(\mathrm{Q}\mathbf{r}+\mathbf{b}\right)\right)^2 \tag{4-1}$$

where $\mathbf{b}$ is the 3D translation motion, f_j is the image at frame j, $\mathbf{r}$ is the discrete 3D spatial coordinate for each voxel center, and Q is the 3D rotation matrix. The sum is taken over all voxels. A total of 6 parameters (3 translational, 3 rotational) are needed to compute E_j. In contrast to other iterative methods, no user-specified parameters or penalty terms are used. Since

the rigid body motion is a smooth vector field which is completely specified by few (6) parameters, and the images contain orders of magnitude more voxels that are being matched, we do not see the need to include any additional penalty terms in the objective function.

The rotation matrix Q may be parameterized by twelve different sets of three Euler angles, where each angle represents a rotation about a Cartesian axis. In each case, specific rotation matrices have multiple distinct parameterizations. This non-uniqueness is due to the dependence of these representations on trigonometric functions. This motivated us to use the quaternion representation which has a unique representation, and only involves simpler algebraic functions [51].

For the reader's convenience we give a brief outline of quaternion-parameterized rotation. See Horn [51] for a more complete treatment. A quaternion q may be viewed as the sum of a scalar and a 3D vector as follows

$$q = \theta_0 + \theta_1 \hat{i} + \theta_2 \hat{j} + \theta_3 \hat{k} \tag{4-2}$$

where $\hat{i}, \hat{j}, \hat{k}$ are unit vectors in 3-space and $\theta_0, \theta_1, \theta_2, \theta_3$ are scalars. q is a unit quaternion if

$$\theta_0^{\,2} + \theta_1^2 + \theta_2^{\,2} + \theta_3^{\,2} = 1 \tag{4-3}$$

The unit quaternion $q = \cos(\omega / 2) + \sin(\omega / 2)\hat{n}$ represents the rotation through the angle ω about the axis parallel to the unit vector $\hat{n}$ (with initial point the origin), where the direction of rotation and $\hat{n}$ form a right-handed system (i.e. ω is the direction of rotation of a right-handed screw being tightened with the tip moving in direction of $\hat{n}$). Thus, we impose the condition $\theta_0 > 0$, which guarantees the unique quaternion parameterization for rotation matrices. So, from equation (4-3), we have $\theta_0 = \sqrt{1 - \left(\theta_1^2 + \theta_2^{\,2} + \theta_3^{\,2}\right)}$. Thus, by using this representation, each

rotation matrix is determined by the unit quaternion vector $\hat{q} = [\theta_1, \theta_2, \theta_3]$ which is explicitly stated in Appendix B, equation (4-B.1). Thus we minimize the objective function in equation (4-1) with respect to the variables $\theta_1, \theta_2, \theta_3, b_1, b_2, b_3$, where $\mathbf{b} = [b_1, b_2, b_3]$.

This minimization was performed by using the modified conjugate gradient algorithm CG_DESCENT developed by Hager and Zhang [53]-[54]. This is a globally convergent nonlinear conjugate gradient method with guaranteed descent and a fast and highly accurate line search technique. As a result, we refer to the proposed method as the CGQ (conjugate gradient quaternion) method.

Experimental Methods

The proposed motion estimation method was compared with three existing methods on two different datasets using both quantitative metrics and visual inspection. In this section we discuss details of implementation of the motion estimation algorithms, how these motion estimates were used to determine a single summed image, the generation of the simulated data and a description of the patient data, and the evaluation methods for the motion obtained from all four methods applied to the two datasets.

Algorithms

We compared our algorithm (CGQ) with the principal axes method [55],[56], the generalized centers of mass method [42], and one which uses the same CG_DESCENT algorithm to minimize the objective function in equation (4-1) but represents the rotation matrix by Euler angles [46] instead of quaternions. Each algorithm was used to minimize E_j in equation (4-1) for j = 2 to j = J, where J is the total number of image frames.

The partial derivatives of (1) used in the CGQ algorithm are given in Appendix C. The CGQ algorithm was initialized with each component of $\hat{q}$ set to zero, and each component of **b**

found by calculating the 3D center of mass in each frame. In the rare case that θ_0 became imaginary, a very large negative number (approaching $-\infty$) was returned for each rotational component of the gradient. The conjugate gradient algorithm (CG_DESCENT) was stopped when the change in the objective function between successive iterations was less than 0.1%.

For comparison to the quaternion method, we implemented three methods that have been used previously for rigid-body motion estimation in medical imaging. These include an iterative conjugate gradient approach and two analytical approaches: principal axes and generalized centers-of-mass.

Instead of using quaternions, methods have been developed based on Euler angle representations of the rotation matrix Q in equation (4-1) [44]-[46]. Here we compare our method with one which uses the "pitch-yaw-roll" system (φ,θ,ψ) corresponding to rotations about the x-axis, the y-axis, and the z-axis, in that order. The rotation matrix and partial derivatives for this system are given in Appendix A. The algorithm was initialized with each rotational component (φ,θ,ψ) set to zero, and each component of **b** found by calculating the 3D center of mass in each frame. The stopping rule was identical to that used in CGQ. We refer to this as the CGPYR (conjugate gradient pitch-yaw-roll) algorithm.

In the principal axes method the translational motion is first estimated by the difference in the centers of mass (COMs) between the reference and deformed frames. Then the deformed frame is translated so that both frames have the same center of mass. The rotational motion is then estimated by the rotation that aligns the principal axes of both frames. This rotation is estimated from analytic relationships between the singular value decompositions (SVDs) of the inertia matrices for the reference and translated deformed frame. This method is not based on iterative algorithms for minimizing an objective function as the CGQ and CGPYR methods, so is

much simpler to implement, but there is no compensation for noise in reconstructed images. The accuracy and speed of this algorithm are very dependent on how the SVDs are computed. In this paper, we used the SVD algorithm of the LAPACK [57] software library (driver routine DSYEVD).

The CGQ algorithm is also compared with the generalized center-of-mass (GCOM) algorithm developed by Feng et al. [42]. By considering the intensity map as a distribution of masses, the center of mass of an image can be computed in terms of the moments of these masses about the coordinate axes. The GCOM method is based on the concept of "generalized center of mass points" which are defined by replacing the (order 1) moment in the usual COM formula, by moments of higher order, $1, 2, 3, \ldots$. For any triplet of orders, the resulting generalized center of mass points are used to estimate the motion by a least squares fitting algorithm. The motion estimates obtained from a finite number of different triplets are then compared using the root-mean-squared distance (RMSD) between the reference and deformed (by the motion estimate) frames. The motion that minimizes this distance (from the finitely many possible motion estimates) is designated to be the motion estimate. Here, we used the code provided by Dr. Bing Feng which is based on the SVD routine taken from the Numerical Recipes software library [58].

Mathematical Phantom Evaluation

Image generation: Tests were performed on an ensemble of 10 noisy realizations of a dual gated (respiratory and ECG binning) cardiac SPECT scan generated by the 4D NURBS-based Cardiac-Torso (NCAT) phantom [59]. Relative organ activity concentrations were based on rest ^{99m}Tc sestamibi studies taken from Gilland et al. [60] and are given in Table I.

To generate realistic motion blur within the ECG gated frames, ECG gating was simulated with 32 frames for one cardiac contraction cycle, and then averaged to a final sampling of 8 frames. Respiratory motion was simulated by rotating and shifting each of the ECG-frames for a total of 32 respiratory-frames per ECG gate. These frames were then averaged to a final sampling of 8 respiratory frames per ECG gate. These transformations resulted in an 8x8 (respiratory cycle bins x ECG bins) matrix of phantom images. The motion used to generate the respiratory frames is given in Table II. These values were taken from human MR studies in McLeish et al. [16] and represent a slightly larger than average displacement. In the table, b_x represents the lateral translation, b_y represents the anterior-posterior translation, b_z represents the cranio-caudal translation, φ represents the rotation about the lateral axis, θ represents the rotation about the anterior-posterior axis, and ψ represents the rotation about the cranio-caudal axis. This notation is identical to that used in CGPYR. Non-rigid deformation of the heart due to respiration was not modeled. Projection data for each of the dual-gated phantom distributions were simulated using the SIMIND Monte Carlo program [61]. Scatter, attenuation, detector stopping power, and detector response were modeled assuming a gamma energy of 140 keV, crystal thickness of 1.27 cm, pixel size of 0.3125 cm, 64 projections over 180º from the left-posterior-oblique to right-anterior-oblique angles, 128×128 detector elements, 15% energy resolution, 20% energy window, and a low energy general purpose parallel-hole collimator. The simulations were allowed to run until noise in the projection data was negligible ($\sigma \approx 2\%$). The data were then scaled to approximately 14,000 total counts in a 3 mm mid-ventricular slice per frame. This count level is typical of a ^{99m}Tc-sestimibi study. Finally, Poisson noise was simulated in each projection set a total of 10 times, generating an ensemble of noise realizations. Each of the noise realizations was reconstructed using 5 iterations of ordered-subsets

expectation-maximization (OSEM) [13] with 8 subsets without attenuation correction. The dual-gated reconstructed images were summed over the ECG frames to generate the 8 respiratory-gated frames upon which the motion estimation methods were tested.

Evaluation metrics: For any motion estimate determined by the rotation matrix $\tilde{Q}$ and the translation vector $\tilde{\mathbf{b}}$, we define the phantom matching error (PME):

$$PME\left(\tilde{\mathrm{Q}},\tilde{\mathbf{b}}\right)=\sum_{j=2}^{J}\sum_{\mathbf{r}}\left(f_{P,1}\left(\mathbf{r}\right)-f_{P,j}\left(\tilde{\mathrm{Q}}_{j}\,\mathbf{r}+\tilde{\mathbf{b}}_{j}\right)\right)^{2} \tag{4-4}$$

where $f_{P,j}$ is the original phantom image without extra-myocardial activity, at frame j. The rotational error is defined as the absolute difference between the estimated rotation and true rotation, in the Euler representation, in degree units. The translational error is defined as the absolute difference between the estimated translation and true translation, in pixel units.

Each of the motion estimation methods was tested on the original, noise-free phantom images without extra-myocardial activity, and on the noisy reconstructed images. Their accuracy was quantified in terms of translational, rotational, and phantom matching errors, each averaged over all eight frames. In the case of the motion estimated from the original phantom images, the PME is a measure of the optimal registration accuracy of each method. The total computation times over all frames were also compared.

The noise-free phantom frames were corrected by translating and rotating frames 2 through 8 based on the estimated motion, and summing with frame 1. The resulting images were evaluated by visual inspection and profile analysis. For comparison purposes, three other images were generated: 1) an uncorrected image, i.e. a summation over the respiratory frames without any motion estimation, 2) an image corrected with the known, true motion, and 3) an ideal image

without any respiration-induced motion (as if the patient held their breath for the duration of the acquisition).

Effect of segmentation: Estimating the respiratory motion of the heart on images with extra-myocardial activity requires segmentation of the myocardial activity due to the non-uniform displacement of organs in the thorax during respiration. To investigate the effects of segmentation on the motion estimation methods, we segmented the left ventricular (LV) wall of the noisy reconstructions over a range of segmentation levels. The different segmentations were created by first varying a 3D Butterworth filter cutoff frequency from 0.32 to 0.64 cycles/cm with a step size of 0.04 cycles/cm. Then, an intensity threshold was varied from 0 to 25% of the maximum pixel intensity with a step size of 2.5%. Pixel values below this threshold were set to zero. This resulted in 99 different segmentations for each noise realization (990 total segmented images). Fig. 4-1 shows 16 of the 99 segmentations for the first noise realization. We can see that as the threshold is increased, less of the extra-myocardial activity is included. The optimal level of segmentation for each method was defined as that which generated the lowest average PME.

Comparison of methods at optimal segmentation: The methods were then compared at the optimal segmentation level for each. The errors were computed as averages over all 10 noise realizations and all 8 respiratory frames. A single noise realization was corrected using the estimated motion from each method, followed by a 3D Butterworth filter of cutoff frequency 0.48 cycles/cm. This level of smoothing was chosen empirically to be comparable to that which we may expect in a clinical setting. The resulting images were evaluated by visual inspection and profile analysis. Again for comparison, an uncorrected, true-motion corrected, and ideal image were also generated.

Effects of varying levels of extra-myocardial activity: In a clinical setting, we would expect to see a high variability in the level of extra-myocardial activity present among patients. The maximum standard deviation of extra-myocardial activity in Gilland et al. [60] was 75%. To test the robustness of the methods under these variable conditions, we calculated the average PME over ten noise realizations for each method at optimal segmentation as the extra-myocardial activity was varied from 0 to 300% (2 ½ standard deviations from average). A single noise realization for 25% and 175% background activity scaling levels was corrected using the motion estimation methods, followed by a 3D Butterworth filter of cutoff frequency 0.48 cycles/cm.

Respiratory-Gated Patient SPECT Images

The methods were further evaluated with a respiratory-gated acquisition of a human subject. The patient was imaged at rest after injection of ^{99m}Tc-sestimibi with a matrix size of 128×128, pixel size of 0.467 cm, with 68 angles over 204° about the left-anterior-oblique angle. Gating of the respiratory cycle was performed using a chest belt as described in section 4.1, with 8 gates per respiratory cycle binned post-acquisition according to phase. The patient dataset was stripped of patient identifiers in compliance with the Health Insurance Portability and Accountability Act (HIPPA)[1].

The data were first reconstructed using 5 iterations of OSEM with 4 subsets. To estimate the respiratory motion, a segmentation of the LV wall was created by first smoothing with a 3D Butterworth filter of cutoff frequency 0.4 cycles/cm, followed by an intensity threshold of 27% of the maximum pixel intensity. A user specified 3D elliptical region-of-interest (ROI) in each frame was drawn around the LV, and all voxels outside this ROI were set to zero. The images

[1] IRB Protocol #157-2004.

were then cropped to a final matrix size of 24×24 with 24 slices. These parameters were chosen empirically, and a transaxial slice of the segmentation at end-expiration is shown in Fig.4-2.

The motion estimation methods were applied to the data, and the resulting motion estimates were used to correct the original, unfiltered reconstruction. This was followed by a 3D Butterworth filter of cut-off frequency 0.37 cycles/cm. This level of smoothing was chosen empirically to be comparable to that which we may expect in a clinical setting. For comparison, an uncorrected image was also created by summing the original, unfiltered reconstructions across the respiratory frames, and smoothing with an identical 3D Butterworth filter of cut-off frequency 0.37 cycles/cm. Since the true motion is not known in these images, the resulting images were evaluated only by visual inspection of myocardial wall blur and uniformity, average objective function value over all frames, and computation time.

Results

All motion estimation methods were implemented on a standard Linux workstation with dual AMD Opteron 250 (2.4 GHz) processors and 4 Gb of memory per processor. In testing, the methods were restricted to execute on a single processor.

Motion Estimation on the Noise-Free Phantom Frames

Results for the motion estimates on the noise-free phantom frames are given in Table III. These results indicate that in terms of accuracy, all correction methods have similar registration and translational errors, but the rotational error for CGQ and principal axes are better than all the other methods. The principal axes method is the computationally fastest followed by GCOM, CGQ, and CGPYR. Note that using the same CG algorithm, but only changing the parameterization of the rotation matrix from the Euler angle representations used in CGPYR and our previous work [46], resulted in a 50% reduction in the computation time.

Fig. 4-3 shows selected short and horizontal views of the noise-free phantom without respiratory motion (ideal), with respiratory motion corrected either by the true motion, CGQ-estimated, or principle axes estimated motion, and with respiratory motion with no correction. CGQ and principal axes corrected images are displayed here because they represent the fastest of the iterative and analytical methods, respectively. The images are shown at the end-diastolic phase of the cardiac contraction motion. The images corrected with CGQ and principal axes are more similar to the image corrected with the true motion in terms of uniformity and sharpness throughout the LV and RV walls, than the uncorrected image. We can see that none of the corrected images achieves the level of myocardial uniformity and sharpness of the ideal image. This may be attributed to the presence of within-frame motion blur as well as interpolation effects inherent in the registration process.

Profiles for the lines shown in Fig. 4-3 are given in Fig. 4-4 for the ideal, CGQ-corrected, and uncorrected images. Profiles for the images corrected with the true motion and principal axes motion were nearly identical to the CGQ profile and thus are not displayed here. The plots show that the corrected images are more similar to the ideal images than the uncorrected images. The corrected profiles are taller, indicating better contrast, and thinner, representing better spatial resolution, than the uncorrected image profiles. Based on the similar accuracy but significantly worse computation time of CGPYR and GCOM to CGQ and principal axes, respectively, these methods were excluded from any further evaluation.

Effect of Segmentation

The results of the segmentation investigation on the reconstructions of the simulated data are shown in Fig. 4-5. The figure shows for the principal axes and CGQ methods a plot of the average PME as a function of intensity threshold and 3D Butterworth cutoff frequency. We can see that CGQ generates a relatively flat and low surface, indicating accurate motion estimation

across a wide range of segmentation levels. The optimal segmentation for CGQ was at threshold = 17.5% and cutoff freq. = 0.44 cycles/cm, generating an average PME of 343.26. Principal axes was highly unstable across the range of segmentations, with optimal segmentation at threshold = 12.5% and cutoff freq. = 0.48 cycles/cm, generating an average PME of 757.23. The differences between the two plots are most profound for thresholds greater than 15%. These levels of segmentation correspond to the top two rows of Fig. 4-1.

Comparison of Methods at Optimal Segmentation

The average motion estimation results for principal axes and CGQ at optimal segmentation over all 10 noise realizations are given in Table IV. CGQ performed significantly better than principal axes in terms of PME accuracy and redundancy (standard deviation) with an average PME of 343.26 ± 100.52. However, the average computation time of CGQ was 55.10 ± 11.13s. The average PME for principal axes was 757.23 ± 158.38, but it again executed on average in under 1s.

Fig. 4-6 shows selected short and horizontal views of the noise-free phantom without respiratory motion (ideal), with respiratory motion corrected either by the true motion, CGQ-estimated, or principle axes estimated motion, and with respiratory motion with no correction. The images are shown at the end-diastolic phase of the cardiac contraction motion. The images corrected with CGQ and principal axes are more similar to the image corrected with the true motion in terms of sharpness throughout the LV walls as well as LV blood pool contrast, than the uncorrected image. Profiles for the lines shown in Fig. 4-6 are given in Fig. 4-7 for the ideal, CGQ-corrected, and uncorrected images. Profiles for the images corrected with the true motion and principal axes motion were again nearly identical to the CGQ profile and thus are not displayed here. The profiles for the corrected images are again more similar to the profiles for

the ideal images than the uncorrected images. Specifically, the corrected image profiles are taller than the uncorrected image profiles, indicating better contrast.

Effect of Varying Level of Extra-Myocardial Activity

In a clinical setting we would expect a large variation in inter-patient extra-myocardial activity levels. Therefore, here we examine how the motion estimation methods behave (at optimal segmentation) as the extra-myocardial activity level is varied. The results for principal axes and CGQ as the background activity levels are varied from 0% to 300% are shown in Fig. 4-8. We can see that the accuracy of CGQ improves as the level of background activity decreases, and worsens as the background levels are increased. However, even as the background activity is increased to 300%, the CGQ-generated motion estimate is still more accurate than a motion estimate of zero for each component (dashed line at 4447.94). This shows good robustness on the part of CGQ over a large range of background activities, as we may expect to see in a clinical setting. In contrast, the principal axes method is highly unstable across the range of background activity levels. Images obtained using principal axes and CGQ at background activity scaling factors of 0.25 and 1.75 (± 1 standard deviation) are shown in Fig. 4-9. The CGQ-corrected images are more similar to the images corrected with the true motion in terms of LV wall uniformity and definition, than the uncorrected images. The images corrected with the principal axes estimated motion are less similar to the images corrected with the true motion than the uncorrected images. An examination of the principal axes motion estimates found that for several frames at each background activity scaling level, the method generated rotational estimates with errors greater than 90°.

Human SPECT Image

The CGQ-corrected, principal axes corrected, and uncorrected human images are shown in Fig. 4-10. We can see that the CGQ-corrected images are more uniform and have decreased

blurring in areas running perpendicular to the axial direction (marked with arrows) compared to the uncorrected image. The principal axes corrected image does not resemble the expected activity distribution. Examination of the motion estimation obtained from principal axes found that two frames had rotational estimates greater than 90°. The average objective function at convergence for CGQ was 431.16. An average objective function value calculated using the principal axes estimated motion was 1368.48. These may be compared to an average objective function of 631.32 calculated using a motion estimate of zero for all components (i.e. no correction). Contrary to the previous studies using the phantom and noisy reconstructions, the computational time for CGQ was 6s. This may be attributed to the larger pixel size of the human study that enabled a small segmented ROI (24x24x24) to be used for the motion estimation. The computation time for principle axes was less than 1s.

Summary and Discussion

In this work, we have developed a new method for respiration-induced cardiac motion correction using a rigid body model with a rotation matrix parameterized by a unit quaternion. The method minimizes an image registration function using an optimized conjugate gradient routine. The implementation uses no user-defined input parameters or prior terms, simplifying the use of the method in a clinical setting. Images corrected with the CGQ-generated motion were found to be more similar to images corrected with the known, true motion compared to uncorrected images on both phantom and simulated data. Our method was also tested on a respiratory-gated study of a human subject. The corrected images have increased uniformity and decreased motion blur in areas of the myocardium running perpendicular to the axial direction. Furthermore, the method was shown to be relatively insensitive to changes in segmentation and extra-myocardial activity level, a key requirement for clinical use. The computation time ranged from 61s on a phantom image to 55.1s on reconstructions of simulated data to 6s on a human

SPECT image. More human studies over a range of detector configurations are needed to determine a typical computation time in routine clinical use, but all of the times reported here are within an acceptable range, especially when hardware acceleration techniques are considered. It should be noted that although consistent improvement between corrected and uncorrected images was found, the difference was not always significant, and it is unclear at this time how respiratory motion correction may impact diagnostic accuracy in cardiac SPECT. Future work will focus on a mathematical observer study as well as a human receiver operating characteristic study on the effects of correcting cardiac respiratory motion blur in cardiac SPECT.

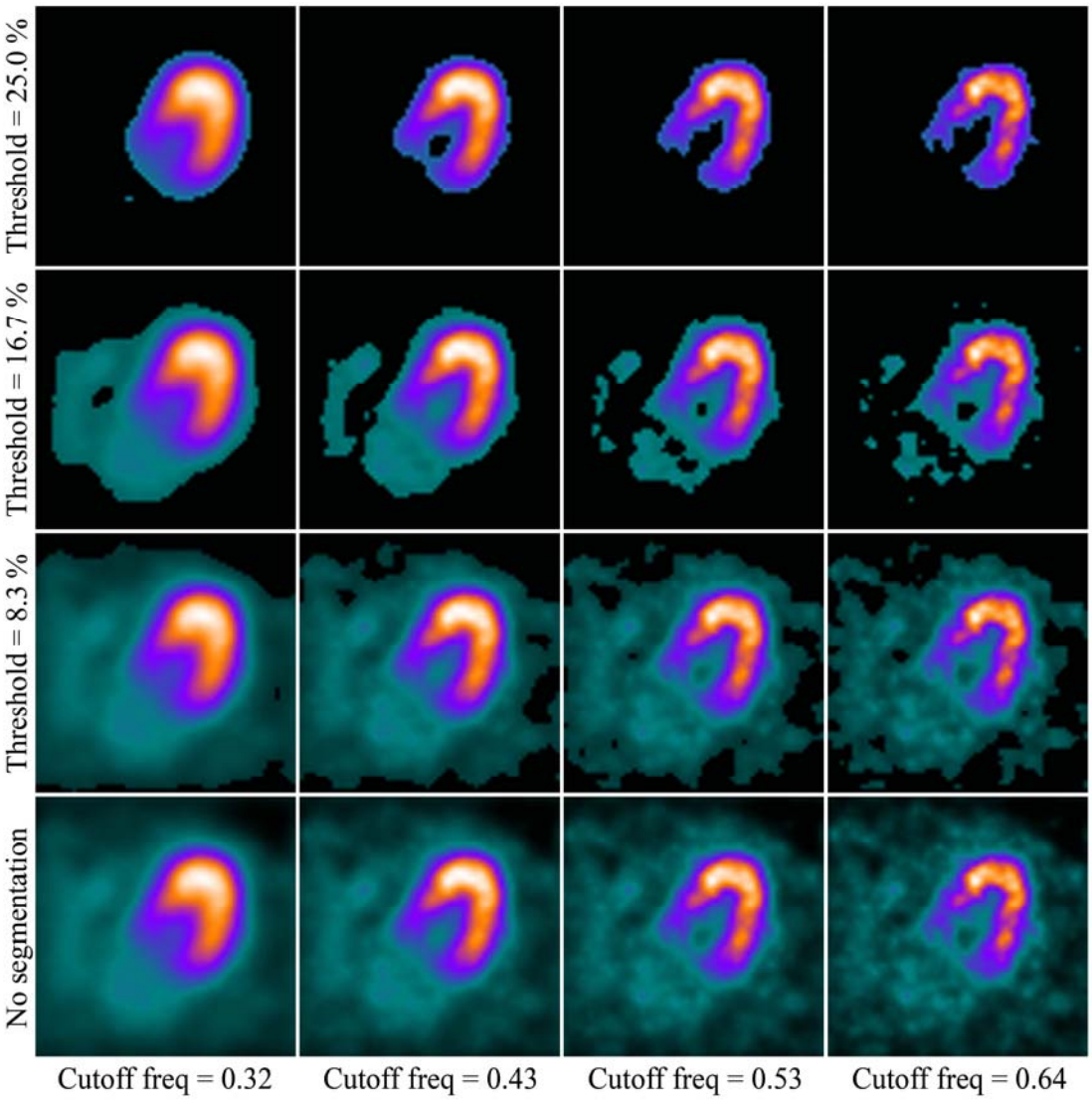

Figure 4-1. Select segmentation levels. The images are summations over the cardiac cycle and shown at end-expiration. Threshold is given in units of percent of maximum pixel intensity, cutoff frequency is given in units of cycles/cm.

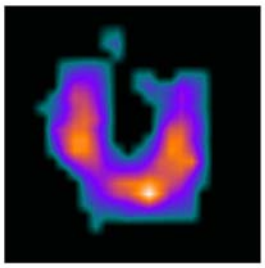

Figure 4-2. Transaxial slice of the segmented human image used for motion estimation (shown at end-expiration).

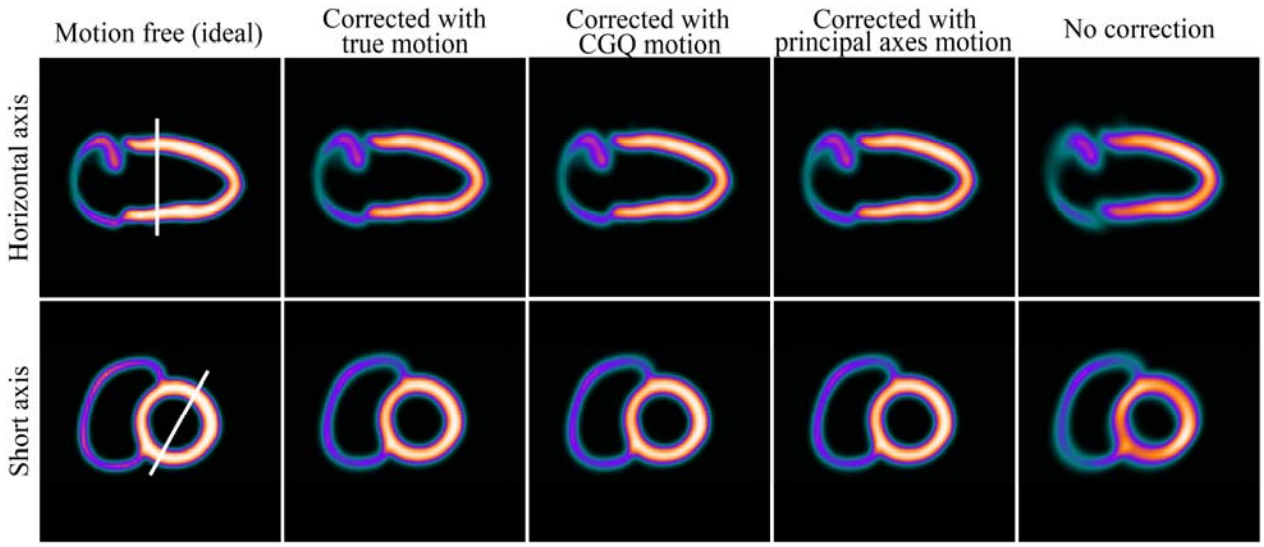

Figure 4-3. Select slices of the phantom images at end-diastole.

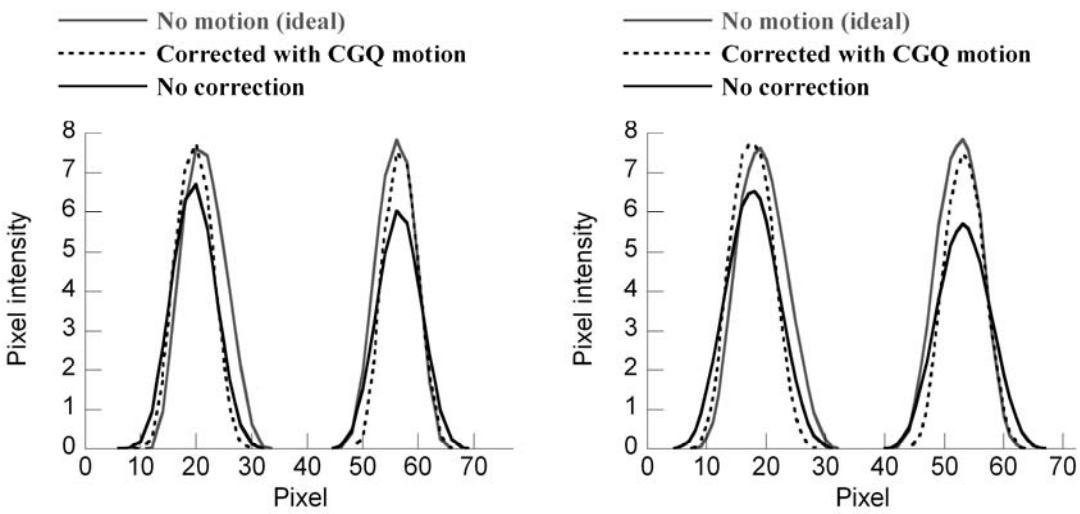

Figure 4-4. Horizontal (left) and short (right) axis profiles for Figure 4-3.

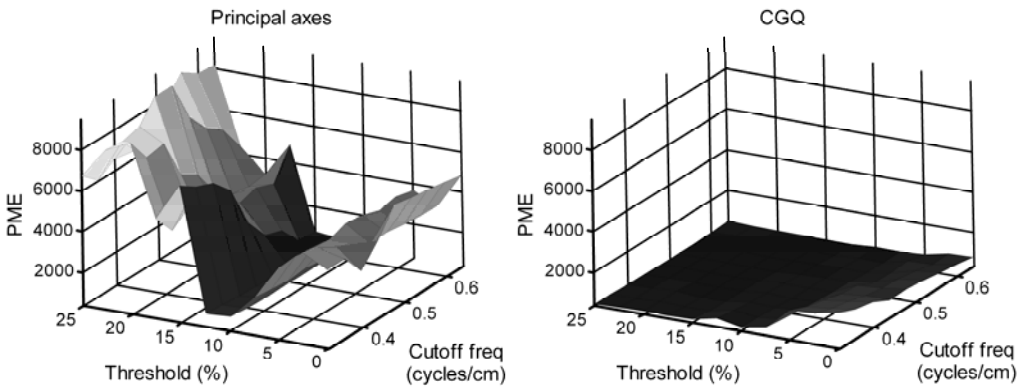

Figure 4-5. Results for average PME found by varying the segmentation parameters. Threshold is given in percentage of maximum pixel intensity, cutoff frequency is given in cycles/cm.

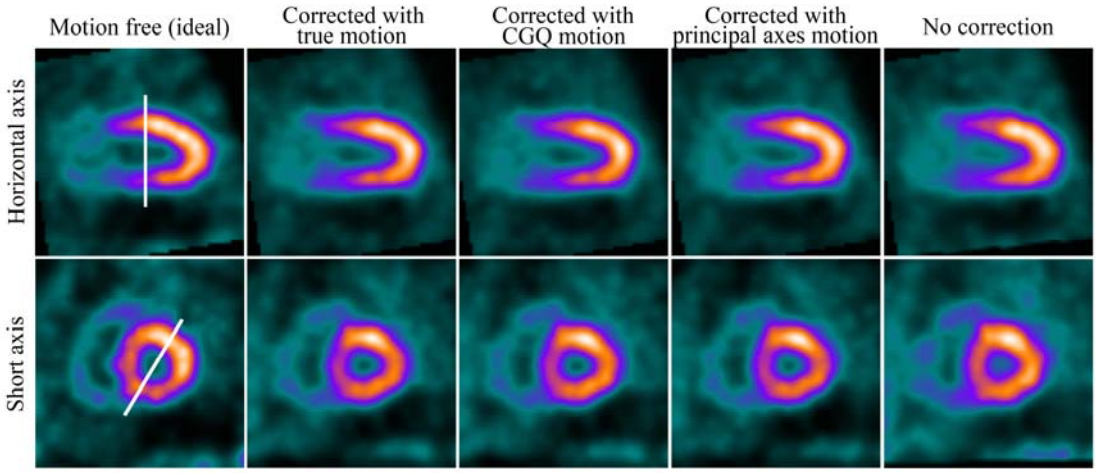

Figure 4-6. Reconstructions of the noisy simulated images at end-diastole

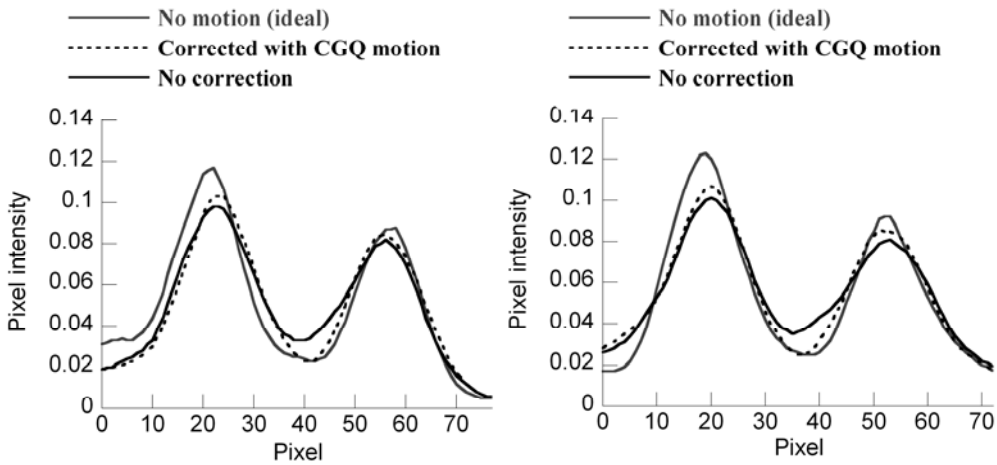

Figure 4-7. Horizontal (left) and short (right) axis profiles for Fig. 4-6.

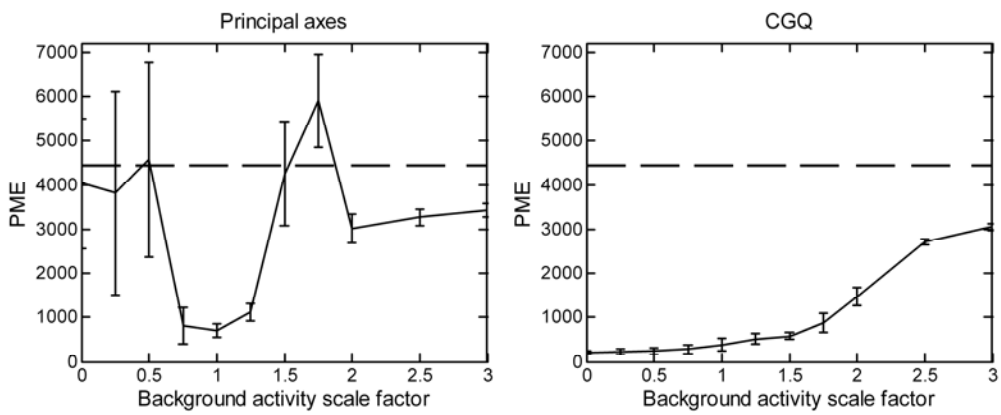

Figure 4-8. Results for average PME found by varying the background activity concentration at optimal segmentation. Error bars indicate the standard deviation of the PME over the ten noise realizations, for each scale factor. The dashed line at 4447.94 represents the PME of an uncorrected image.

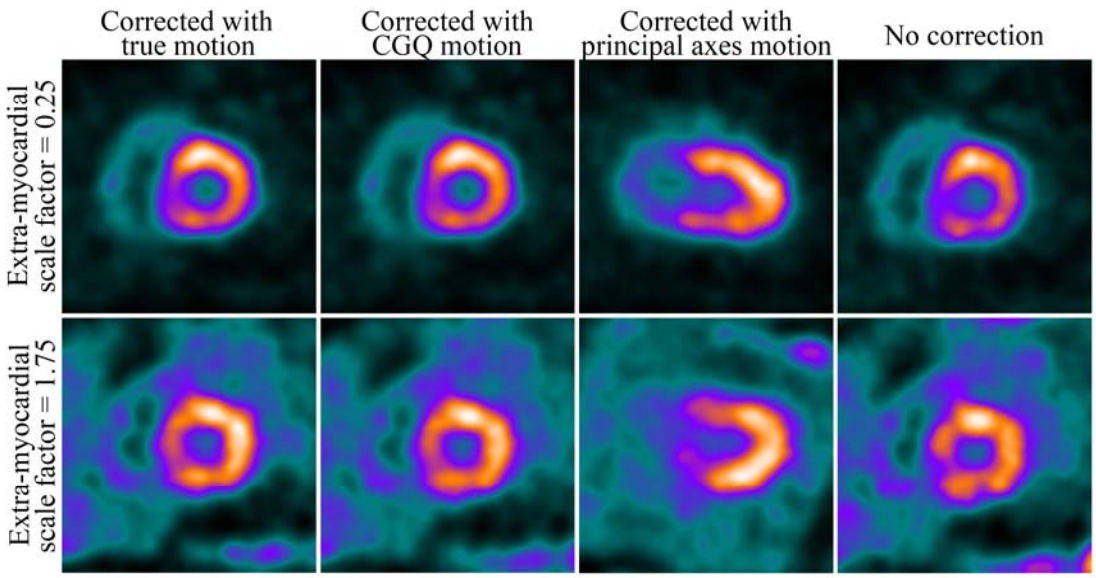

Figure 4-9. Reconstructions of the simulated data at extra-myocardial activity levels of 0.25 and 1.75 (fraction of average). CGQ-corrected images are nearly indistinguishable from images corrected with the true motion.

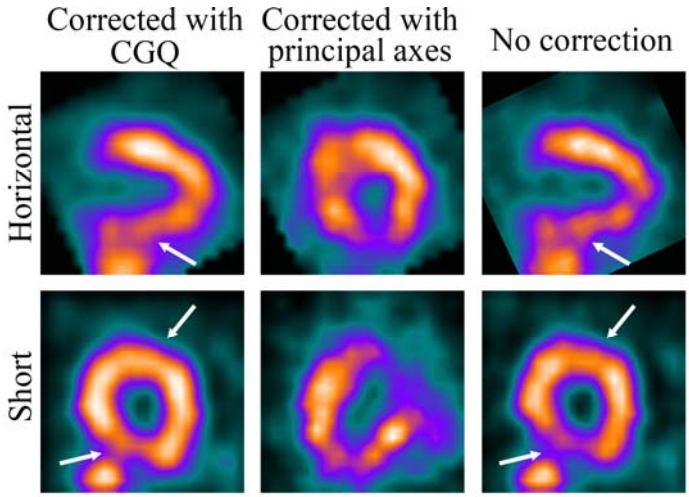

Figure 4-10. Reconstructions of the human images with CGQ correction, principal axes correction, and no correction, respectively. The CGQ-corrected image has increased uniformity and sharpness in areas perpendicular to the axial motion (marked with arrows) compared to the uncorrected image.

Table 4-1. Relative organ activity concentrations for the simulated NCAT phantom

Organ	Relative activity
Myocardium	75
Heart blood pool	6
Liver	13
Gall bladder	324
Lung	6
Kidney	45
Spleen	45
Bowel	37
Background (body)	6

Table 4-2. Respiratory motion in the mathematical phantom images relative to frame 1. Translations are given in pixels, rotations in degrees.

Frame interval	b_x	b_y	b_z	ψ	φ	θ
1→1	0.0	0.0	0.0	0.0	0.0	0.0
1→2	-0.28	-0.864	-0.96	-1.675	-1.65	-0.375
1→3	-0.56	-1.728	-1.92	-3.35	-3.3	-0.75
1→4	-0.84	-2.592	-2.88	-5.025	-4.95	-1.125
1→5	-1.12	-3.456	-3.84	-6.7	-6.6	-1.5
1→6	-0.84	-2.592	-2.88	-5.025	-4.95	-1.125
1→7	-0.56	-1.728	-1.92	-3.35	-3.3	-0.75
1→8	-0.28	-0.864	-0.96	-1.675	-1.65	-0.375

Table 4-3. Motion estimates from the noise-free phantom images

Method	Translational error (pixels)	Rotational error (degrees)	PME	Computation time (s)
CGQ	0.15	0.01	100.03	61.00
CGPYR	0.15	0.15	100.03	119.72
Principal axes	0.15	0.01	100.81	0.13
GCOM	0.14	0.36	107.96	54.59
No correction	1.4	2.5	4447.94	-

Table 4-4. Average motion estimation errors for the 10 noisy simulated images with background activity at optimal segmentation

Method	Translational error (pixels)	Rotational error (degrees)	PME	Computation time (s)
CGQ	0.24 ± .05	1.05 ± .16	343.26 ± 100.52	55.10 ± 11.13
Principal axes	0.31 ± .07	2.25 ± .42	757.23 ± 158.38	0.08 ± .04
No correction	1.4	2.5	4447.94	-

CHAPTER 5
SIMULTANEOUS IMAGE RECONSTRUCTION AND MOTION ESTIMATION IN GATED CARDIAC EMISSION TOMOGRAPHY: A MATHEMATICAL OBSERVER STUDY

Introduction

In this chapter, we evaluate the image quality of the simultaneous image reconstruction and motion estimation method compared to a standard reconstruction method in terms of a binary lesion detection task in SPECT myocardial perfusion imaging. ECG-gated source distributions of a normal human torso and a myocardial perfusion defect were simulated using a mathematical cardiac torso phantom. Projection data were obtained from the source distributions using a Monte Carlo code which modeled the effects of scatter, attenuation, and detector response. A total of 500 noise realizations for each projection set (500 normal, 500 abnormal) were reconstructed using the simultaneous image reconstruction and motion estimation method and a post-smoothed ordered-subsets expectation-maximization (PS-OSEM) [13] reconstruction. A channelized Hotelling observer [21],[62] was formulated to operate on single short axis slices (CHO), as well as on the complete multi-frame images (MACHO) [63]-[64].

During the study we noticed an inconsistency between the CHO and human observers in that the optimal level of smoothing for the CHO corresponded to Butterworth cutoff frequencies less than 0.05 cycles/pixel. Because we felt that an evaluation of the methods at such high levels of smoothing would not necessarily predict the relative performance of the methods in a clinical setting, we chose to adjust the reconstruction parameters for RM and PS-OSEM such that the methods produced images with spatial resolution characteristics typical of clinical images. The CHO was then used to generate an ensemble of test statistics for each reconstruction method, and a receiver operating characteristics methodology was used to analyze the statistical ensembles. The area under the ROC curve (AUC) was used as an image quality figure of merit, and the statistical significance of the difference between the ROC estimates was determined.

The signal-to-noise ratio (SNR) for each method was also calculated directly using a regions-of-interest technique across the ensemble data. The statistical significance of the difference in SNR between RM and PS-OSEM using the regions-of-interest method was evaluated using a paired t-test.

Background

Motion Compensated Image Reconstruction

It has been shown that including non-rigid motion estimation in the penalty term of a maximum a posteriori (MAP) reconstruction can improve the noise properties of reconstructed gated images while retaining a low level of motion blur [9],[10],[12],[24],[65]. The idea was first investigated in Lalush et al. [9] where the authors modeled the motion of a mathematical beating heart as an ellipsoid undergoing affine transformations. The process involved two steps: 1) motion estimation based on general known properties of the human heart followed by, 2) a reconstruction of the gated images using the estimated motion vectors as Gibbs priors in a MAP reconstruction. The authors found that clique weights based on the estimated motion vectors generated by the affine motion model enforced better spatial resolution and comparable noise levels compared to several other “no-motion” families of Gibbs priors.

In Gravier et al. [24] a similar approach was used except that the authors generated their estimated motion vector field by using the 2D optical flow method of Horn and Schunck [29] on initial filtered backprojection (FBP) reconstructions of the gated images. In Gravier et al. [65] the authors extended their method to 3D and evaluated the resulting images in terms of lesion detection using a channelized Hotelling observer. It was found that the 4D motion compensated images had superior lesion detection properties compared to images without temporal smoothing. However, in both [24] and [65] the authors noted that the accuracy of the non-rigid motion

vector fields used in their MAP reconstructions suffered from the already high noise levels of the FBP images.

Simultaneous Image Reconstruction and Motion Estimation

Motivated by the inherent problem of high-noise motion estimation in [24] and [65], a method which simultaneously estimates both the tomographic images and non-rigid motion vector fields has been proposed [10],[12],[66]. The method is described by the following objective function:

$$E(\mathbf{f},\mathbf{m}) = \alpha L(\mathbf{f}) + E_I(\mathbf{f},\mathbf{m}) + \beta E_S(\mathbf{m}) \tag{5-1}$$

where **f** is the 4D tomographic image, **m** is the 4D motion vector field,

$$L(\mathbf{f}) = \sum_{j=1}^{J}\sum_{i=1}^{p}\left[Hf_j(i) - g^{(j)}(i)\log Hf_j(i)\right] \tag{5-2}$$

is the negative log likelihood of obtaining the detector data from the reconstructed image **f**, $Hf(i)$ is the projection operator, **g** is the measured detector data vector, J is the total number of frames, p is the total number of detector bins,

$$E_I(\mathbf{f},\mathbf{m}) = \sum_{j=1}^{J}\sum_{\mathbf{r}}\left[f_j(\mathbf{r}) - f_{j+1}\left(\mathbf{r}+\mathbf{m}_j(\mathbf{r})\right)\right]^2 \tag{5-3}$$

is an image registration term taken over all voxels **r**,

$$E_s(\mathbf{m}) = \sum_{j=1}^{J}\sum_{\mathbf{r}}\left(\left|\nabla u_j(\mathbf{r})\right|^2 + \left|\nabla v_j(\mathbf{r})\right|^2 + \left|\nabla w_j(\mathbf{r})\right|^2\right) \tag{5-4}$$

is *a priori* information about the object motion (in this case a smoothness constraint on the estimated motion vector field), u,v,w are the components of the estimated motion vector field **m**, and ∇ is the gradient operator. In eq. 5-1 α and β are user-defined scalars which control the influence of the reconstruction and motion smoothing terms, respectively. It should be noted that E_s can be used to enforce more stringent models of the object motion such as incompressibility,

consistency with a prediction field, or (as in Mair et al. [12]) the strain energy of a material undergoing elastic deformation. This simultaneous method has been shown to have improved motion estimation properties compared to a standard motion estimation method [67], as well as improved image quality compared to a standard reconstruction method in an SSE (eq. 3-1) sense [12]. However, an investigation of the detection properties of the simultaneous method has been notably absent from previous studies.

Channelized Hotelling Observer

Receiver operating characteristics studies using human observers are considered the gold standard in evaluating the detection properties of imaging modalities [20]. However, these studies are time consuming and require the participation of multiple observers. An alternative to human studies are mathematical observers designed to mimic the detection properties of humans [68]. The channelized Hotelling observer is one such model observer with a channel operator developed to model the human visual system. The method has been shown to correlate well with human observers in relatively difficult imaging tasks with both correlated noise and random backgrounds [62]. A brief description of the channelized Hotelling observer is given here; a more detailed description can be found in Yao and Barrett [21] and Myers and Barrett [62].

The CHO uses a set of training images to build a covariance matrix which describes the statistical differences between signal absent (SA) and signal present (SP) classes. It has been suggested that the number of images used for training should be at least equal to the order of the covariance matrix. After the covariance matrix has been generated, the CHO can calculate a test statistic for a given image which can be compared to a decision threshold to classify the image as normal or abnormal. What separates the CHO from other mathematical observers (e.g. the non-prewhitening observer) is a pre-filter process which models the human visual system by operating on the power of select frequency bands, rather than the full frequency spectrum. This

pre-filter stage is referred to as a channel mechanism and it's inclusion into the Hotelling observer has demonstrated good correlation with human observers [69]-[71].

We represent each of the reconstructed images as a 1D vector, $\vec{g}$, of length *N*. The CHO test statistic, λ_{CHO}, is defined as:

$$\lambda_{CHO} = \left(\bar{\vec{v}}_{SP} - \bar{\vec{v}}_{SA}\right)^T S_{2\vec{v}}^{-1} \bullet \vec{v} \tag{5-5}$$

where $\bar{\vec{v}}_{SP}$ is the mean feature vector of a set of SP images, $\bar{\vec{v}}_{SA}$ is the mean feature vector of a set of SA images, *T* is the transpose operator, S_{2v}^{-1} is the inverse of the average inter-class scatter matrix (S_{2v}), and $\vec{v}$ is the feature vector of the current image. The average inter-class scatter matrix is defined by:

$$S_{2\vec{v}} = \frac{1}{2}\left(S_{\vec{v},SP} + S_{\vec{v},SA}\right) \tag{5-6}$$

where $S_{\vec{v},i}$ is the average intra-class scatter matrix, defined by:

$$S_{\vec{v},i} = \left\langle \left(\bar{\vec{v}} - \bar{\vec{v}}_i\right)\left(\bar{\vec{v}} - \bar{\vec{v}}_i\right)^T \right\rangle_i \tag{5-7}$$

where the $\langle\ \rangle$ operator represents an average over class *i*. The CHO operates using a number of frequency bands, *L*. The feature vector $\vec{v}$ is defined by:

$$\vec{v} = U\vec{g} \tag{5-8}$$

where U is the LxN channel operator matrix. We use 4 rotationally symmetric frequency bands or "channels," with each band one octave wide ranging from 0.03125 to 0.0625 cycles/pixel, 0.0625 to 0.125 cycles/pixel, 0.125 to 0.25 cycles/pixel, and 0.25 to 0.5 cycles/pixel. Fig. 5-1 shows a plot of the four channels. These channels have been shown to correlate well with human observers [71]. The feature vector *v* can be calculated in either the frequency or spatial domain; here we use the spatial domain approach to avoid taking a large number of Fourier transforms.

Spatial domain templates for U may be calculated by taking the inverse Fourier transform of the frequency bands. The spatial domain templates may then be used each time v is calculated. The frequency bands and their corresponding spatial domain templates are shown in Fig. 5-2. In this paper, the center of the defect must be aligned with the center of the spatial domain template. All images were scaled to integer intensities between 0 and 255 to mimic the conditions of a human ROC study.

The CHO SNR *d'* may be used as an image quality figure of merit:

$$d'_{CHO} = \sqrt{\frac{2\left(\bar{\lambda}_{SP} - \bar{\lambda}_{SA}\right)^2}{\mathbf{var}\left(\lambda_{SP}\right) + \mathbf{var}\left(\lambda_{SA}\right)}} \tag{5-9}$$

where $\bar{\lambda}_{SP}$ is the mean of λ_{CHO} given class SP, $\bar{\lambda}_{SA}$ is the mean of λ_{CHO} given class SA, $\mathrm{var}\left(\lambda_{SP}\right)$ is the variance of λ_{CHO} within class SP, and $\mathrm{var}\left(\lambda_{SA}\right)$ is the variance of λ_{CHO} within class SA. The area under the ROC curve (AUC) is related to *d'* by:

$$\mathrm{AUC} = \frac{1}{2} + \frac{1}{2}\mathrm{erf}\left(\frac{d'}{2}\right) \tag{5-10}$$

where **erf** is the Gaussian error function for *d'*:

$$\mathrm{erf}(d') = \frac{2}{\sqrt{\pi}}\int_0^{d'} e^{-t^2}\,dt \tag{5-11}$$

Multiple-Array Channelized Hotelling Observer

In Chen et al. [63] it was hypothesized that in a clinical setting, human observers would consider both multiple slices and multiple views in the detection process, and that a CHO modeling this behavior would reflect human observers more accurately. The authors provided a mathematical framework to extend the CHO to operate on 4D images. However, the authors did

not find a significant difference in correlation with human observers when using the 4D approach compared to the 2D approach.

More recently our group has developed an extension of the CHO for use in gated imaging [64] that is based on the framework provided by Chen et al. [63]. The difference between our method and that of [63] is that we operate on multiple frames, as opposed to multiple slices and multiple views. We propose the use of this method for ECG-gated tomographic image sets because it takes into account the full series of gated images, more closely modeling a clinical evaluation. We refer to the method as the multiple-array channelized Hotelling observer (MACHO).

The first step of the MACHO is to calculate the usual CHO test statistic for each 2-D slice of each image frame. This results in a vector of test statistic, $\vec{\lambda}_{CHO}$, of length N_λ for each noisy reconstructed image. In this study a single short axis slice through the center of the lesion location in each image frame was used, and thus N_λ was equal to the number of ECG-gated frames. The second step uses a Hotelling observer (HO) to generate an overall test statistic, Λ_{MACHO}, for each noisy reconstruction, from the collection of CHO test statistics $\vec{\lambda}_{CHO}$. The HO is similar to the CHO, but without the pre-filtering stage:

$$\Lambda_{MACHO} = \left(\bar{\vec{\lambda}}_{CHO,SP} - \bar{\vec{\lambda}}_{CHO,SA} \right)^T S^{-1}_{2\vec{\lambda}_{CHO}} \bullet \vec{\lambda}_{CHO} \tag{5-12}$$

where $\bar{\vec{\lambda}}_{CHO,SP}$ is the mean vector of $\vec{\lambda}_{CHO}$ over all SP training images, $\bar{\vec{\lambda}}_{CHO,SA}$ is the mean vector of $\vec{\lambda}_{CHO}$ over all SA training images, $S^{-1}_{2\vec{\lambda}_{CHO}}$ is the inverse of the average inter-class scatter matrix ($S_{2\vec{\lambda}_{CHO}}$), and $\vec{\lambda}_{CHO}$ is the vector containing a λ_{CHO} for each slice of the current image. The average inter-class scatter matrix is defined by:

$$S_{2\vec{\lambda}_{CHO}} = \frac{1}{2}\left(S_{\vec{\lambda}_{CHO},SP} + S_{\vec{\lambda}_{CHO},SA}\right) \tag{5-13}$$

where $S_{\vec{\lambda}_{CHO},i}$ is the average intra-class scatter matrix, defined by:

$$S_{\vec{\lambda}_{CHO},i} = \left\langle \left(\vec{\lambda}_{CHO} - \bar{\vec{\lambda}}_{CHO,i}\right)\left(\vec{\lambda}_{CHO} - \bar{\vec{\lambda}}_{CHO,i}\right)^T \right\rangle_i \tag{5-14}$$

The MACHO SNR, d', is defined as:

$$d'_{MACHO} = \sqrt{\frac{2\left(\bar{\Lambda}_{SP} - \bar{\Lambda}_{SA}\right)^2}{\mathbf{var}\left(\bar{\Lambda}_{SP}\right) + \mathbf{var}\left(\bar{\Lambda}_{SA}\right)}} \tag{5-15}$$

Methods

Simulation of Test Data

The 4D NURBS-based Cardiac Torso (NCAT) phantom [59] was used in this study. An activity distribution representing an ECG-gated ^{99m}Tc-Sestamibi rest SPECT scan of a normal (defect-free) human torso was generated with 32 frames over one complete cardiac contraction cycle. Relative organ activity concentrations were taken from Gilland et al. [60] and are given in Table 5-1. The 32 frames were then down-sampled to 8, providing realistic within-frame motion blur in the ECG gated images.

Additionally, an activity distribution representing a myocardial perfusion defect was generated. The defect, shown in Fig. 5-3 (after subtracting from the normal activity distribution), had a circumferential width of 120°, length of 31.25 mm, and transmural thickness equal to the thickness of the myocardium. This defect is considered to be a large sized defect [72]. The cardiac contraction motion for the defect was sampled at 32 frames and down-sampled to 8.

The SIMIND Monte Carlo program [61] was used to generate realistic projection data from the normal activity distribution and the defect activity distribution, separately. After the simulation, the defect projection data could be subtracted from the normal projection data to

create a projection data set with a myocardial perfusion defect. The simulations of the normal and defect projection data were carried out separately to avoid simulating the extra-myocardial activity (a time consuming procedure) more than once. Also, separate simulations made it possible to adjust the defect contrast in the evaluation of the CHO code (section 5.2.C). Scatter, attenuation, detector stopping power, and detector response were modeled in both simulations assuming a gamma energy of 140 keV, crystal thickness of 1.27 cm, pixel size of 0.3125 cm, 64 projections over 180º (LPO to RAO), 128x128 detector elements, and a low energy general purpose parallel hole collimator (3mm across hexagonal holes with 4.2mm pitch). The simulations were allowed to run until noise in the projection data was negligible ($\sigma \approx 2\%$). OSEM reconstructions of the noise-free projection data with and without the defect are shown in Fig. 5-4. In the figure, the pixel intensity in the location of the defect is scaled to 95% of the normal myocardial wall pixel intensity (referred to as a 5% defect).

Validation of the CHO

Prior to the comparison of RM and PS-OSEM, we tested the CHO across a wide variety of reconstructed images. The purpose of this step was to ensure the code could be used as an indicator of image quality. Six tests were performed. Each test used 500 noise realizations of SP and 500 noise realizations of SA data with reconstruction using 5 iterations of OSEM with 8 subsets.

Test 1: The CHO SNR (eq. 5-9) across a variety of defect intensities was tested. The defect projection set was scaled from 50% to 97.5% of the intensity of the normal myocardial wall and subtracted from the normal projection set, creating projection sets with myocardial perfusion defects ranging from 2.5% to 50%. The intensities of the projection sets were then scaled to 14,000 counts/frame within a 3mm mid-ventricular slice, and Poisson noise was simulated. This count level is representative of a clinical rest SPECT scan using ^{99m}Tc-Sestamibi

and for this paper will be referred to as the "clinical count level." The images were smoothed with a 3D Butterworth filter with cut-off frequency equal to 0.15 cycles/pixel. This level of smoothing was chosen to be representative of that which we would find in a clinical setting [73]. The response of the CHO across the range of defect contrasts was analyzed using eq. (5-9).

Test 2: The CHO SNR across a variety of noise levels was tested. A projection set with a single 25% defect was generated, and the total intensity was scaled (from the clinical count level) by factors of 0.1 to 1.5. This scaling was followed by simulated Poisson noise. At each level of scaling the images were smoothed with a 3D Butterworth filter with cut-off frequency equal to 0.15 cycles/pixel, and the CHO SNR was calculated using eq. (5-9).

Test 3: The response of the CHO SNR to the number of channels used was tested. A set of reconstructed images with a single 25% defect at the clinical count level were used to test the CHO with the number of channels used ranging from 1 to 4.

Test 4: The response of the CHO SNR to the number of training images used was tested. This test was used to ensure that the number training images used in the ROC evaluation would yield statistically significant results. A set of reconstructed images with a single 25% defect at the clinical count level were used to test the CHO with training image quantities ranging from 10 to 250.

Test 5: The response of the CHO SNR to varying levels of spatial smoothing was tested. A set of reconstructed images with a single 25% defect and the clinical count level was tested with a 3D Butterworth filter with cut-off frequency ranging from 0.0 to 0.3 cycles/pixel.

Test 6: The response of the CHO SNR to varying levels of temporal smoothing was investigated. A set of reconstructed images with a single 25% defect and the clinical count level was tested with a 3D Butterworth filter with cut-off frequency 0.15 cycles/pixel and a 3-point

temporal convolution over a range of kernel weights. The temporal smoothing kernels are defined in Table 5-2.

Image reconstruction

For the comparison of the RM and PS-OSEM methods, a set of 500 SA and 500 SP projection sets at the clinical count level were created from the noise-free simulations. The SP sets had a 5% defect. Based on the results of *Test 5* and *Test 6* in section 5.2.C, we chose to evaluate the RM and PS-OSEM methods at equal levels of spatial resolution. The spatial resolution was quantified as the full-width at half-maximum (FWHM) of a profile through the left-ventricular wall of a noise-free, defect-free reconstruction in the short axis view. To ensure this was a valid measure of spatial resolution, it was tested on MLEM images as a function of MLEM [11] iteration number, 3D Butterworth cut-off frequency, and temporal convolution kernel.

PS-OSEM reconstruction: For the PS-OSEM reconstructions, a spatial resolution level similar to clinical images was defined as 5 iterations of OSEM with 8 subsets followed by a 3D Butterworth filter with a cut-off frequency of 0.15 cycles/pixel [73] and a 3-point temporal convolution with weights {.25,.5,.25} (temporal convolution kernel #4). The FWHM of a noise-free PS-OSEM image at this spatial resolution was calculated. These settings were then used to reconstruct the 500 noise realizations of SA and SP projection sets.

RM reconstruction: In this paper the reconstruction-step (R-step) of RM was a MAP reconstruction which used a modification of Green's one step late algorithm [74]. The implementation of the R-step is detailed in Mair et al. [12]. The motion-step (M-step) in this paper was a generalization of the Horn and Schunck optical flow algorithm into a sequential quadratic framework [75]. The parameters α and β were determined empirically using a noise-

free SA projection set to generate a spatial resolution equal to the PS-OSEM images. These settings were then used to reconstruct the 500 noise realizations of SA and SP projection sets.

ROC evaluation

The CHO was used to generate a set of test statistics for both reconstruction methods. The CHO test statistics were calculated using a central slice (through the defect center) at the end-diastolic frame of the gated reconstructions. The ROCKIT software package developed at the University of Chicago [20] was used to generate a maximum likelihood estimation of the parameters of the bivariate binormal ROC model for the paired data as well as to calculate the statistical significance of the difference between the binormal ROC curve estimates.

An identical study was also performed using the MACHO in place of the CHO. The MACHO test statistics were calculated using a central slice of all frames (8) of the gated reconstructions.

Direct assessment of SNR using regions-of-interest across the ensemble data

The SNR for both RM and PS-OSEM was also calculated directly using a regions-of-interest technique [76] across the SP ensemble data. The average pixel intensity in the area of the defect, L, was calculated using a region-of-interest defined by the margins of the defect (Fig. 5-5) in the central slice of the end-diastolic frame. Then, in three consecutive slices of the end-diastolic frame, two regions-of-interest with shape identical to the defect ROI were defined within the myocardial activity but outside the area of the defect. The average pixel intensity of each lesion-free ROI, b_i, was calculated (where i=1,2,…,6). The SNR was then defined as:

$$SNR_{ROI} = \frac{B - L}{\sigma_{b_i}} \tag{5-16}$$

where B is the average of b_i, and σ_{b_i} is the standard deviation of b across all i. The final value of the SNR_{ROI} for both RM and PS-OSEM was computed as an average over the ensemble of SP

data (500 noise realizations). The significance of the difference in SNR_{ROI} between the RM and PS-OSEM methods was evaluated using a paired t-test. For comparison to the results of *Test 5* using the CHO, the response of the SNR_{ROI} was also tested across a range of 3D Butterworth cut-off frequencies.

Reconstruction without the effects of scatter , attenuation, and detector response

We also compared the RM and PS-OSEM methods qualitatively using projection data obtained from the phantom by a simple linear projector that ignored the effects of scatter, attenuation, and detector response. Poisson noise at the clinical count level was simulated in the projection set and RM and PS-OSEM reconstruction parameters were optimized using the SSE (eq. 3.1) between the original, noise-free phantom and the reconstructed images.

Results

Validation of the CHO

Test 1: Fig. 5-6 shows the results found by testing the CHO at different levels of defect contrast. The figure shows the CHO SNR increases as the defect contrast is increased. This is in agreement with previous studies [72] and validates the code's ability to rank image quality in terms of defect detection.

Test 2: Fig. 5-7 shows the results found by testing the CHO at varying count levels. The plot shows that the CHO SNR increases as the total counts increase. This is in agreement with our expectation that detection should improve as image noise improves. The study further supports the code's ability to rank image quality in terms of defect detection.

Test 3: Fig. 5-8 shows the results of varying the number of channels used by the CHO from 1 to 4. As expected as the number of channels increases, the CHO SNR also increases. This is due to the inclusion of more information as more channels are used.

Test 4: Fig. 5-9 shows the results found by varying the number of images used for training. There is a sharp incline in SNR between 10 and 30 images, after which point the plot levels out. We would expect a sharp incline between 0 and 16 images, which is the order of our covariance matrix. However, several authors have pointed out that although this rule of thumb guarantees the existence of the inverse scatter matrix, it often underestimates the number of images needed for a statistically significant study [77]-[80], which may explain the continued increase up to ~30 training images.

Test 5: Fig. 5-10 shows the results of the CHO SNR versus Butterworth cut-off frequency. There is a sharp increase in SNR between cut-off frequencies of 0. and 0.025 cycles/pixel, followed by a gradual and consistent decrease. Images representing four sample points in Fig. 5-10 are shown in Fig. 5-11. It is clear from the images that the level of smoothing which generates the highest CHO SNR (cut-off = 0.025 cycles/pixel) is considerably smoother than typical clinical images. These results do not agree with those reported in Frey et al. [72]; however, a similar discrepancy was noted by another author [81]. Because the level of spatial smoothing is not normally optimized in papers using the CHO, at this time it is unclear if the results of this test are unique.

Test 6: Fig. 5-12 shows the results of the CHO SNR versus temporal smoothing kernel. The results display a steady increase in CHO SNR as temporal smoothing weights are increased. This is in agreement with the findings of *Test 5*. Images representing the 5 levels of temporal smoothing are shown in Fig. 5-13.

Image Reconstruction

The results of the FWHM versus MLEM iteration number investigation for noise-free data are shown in Fig. 5-14. As expected the spatial resolution of the image improves rapidly with the first few MLEM iterations (iterations 1-10) but then begins to level off (iterations 20-

50). Fig. 5-15 shows the results of the FWHM versus Butterworth cut-off frequency. The spatial resolution again improves rapidly at first but then begins to level off. Figure 5-16 shows the results of FWHM versus temporal smoothing kernel. The spatial resolution degrades as the level of temporal smoothing is raised. These experiments validated the use of the FWHM of the LV wall to quantify the level of spatial resolution in the images. The FWHM of the PS-OSEM image after 5 iterations of OSEM with 8 subsets, Butterworth filter with cut-off frequency 0.15 cycles/pixel, and temporal convolution kernel number 4 was 60.5 pixels. The RM parameters found to yield an equivalent FWHM were α=0.13 and β=0.05. Example images for the PS-OSEM and RM reconstructions of the noise free data and their corresponding profiles are shown in Fig. 5-17. The estimated motion vector fields generated by RM on the noise-free data are shown in Fig. 5-18. The vector fields demonstrate a good balance between motion magnitude and motion smoothness.

Example reconstructed images for the RM and PS-OSEM methods used in the CHO and MACHO study are shown in Fig. 5-19. The PS-OSEM images appear to have better contrast and uniformity of the activity distribution compared to the RM images. This is in contrast to results found in previous papers which used simpler models of the system matrix and phantom object and higher spatial resolution in the reconstructed images [10],[12],[66].

ROC Evaluation

The ROC curve generated using the CHO is shown in Fig. 5-20. The curve for PS-OSEM stays above RM at all areas of the plot, representing superior detection regardless of threshold effects. The AUC for RM was 0.69, compared to 0.72 for PS-OSEM. The p-value calculated from the correlated bivariate chi-square test statistic was 0.54 (46% confidence level). This result demonstrates that when using a single short-axis slice, it cannot be said that the detection of the RM and PS-OSEM methods differs.

Fig. 5-21 shows the ROC curve generated using the MACHO. In contrast to Fig. 5-20, the RM curve stays above PS-OSEM at all areas of the plot. The AUC for RM was 0.85, compared to 0.83 for PS-OSEM. The p-value calculated from the correlated bivariate chi-square test statistic was 0.80 (20% confidence level). This result demonstrates that when considering all frames of a gated image, it cannot be said that the detection characteristics of the RM and PS-OSEM methods differ.

Direct Assessment of SNR Using Regions-of-Interest across the Ensemble Data

The signal-to-noise ratios (SNR_{ROI}) calculated using the regions-of-interest technique were 0.50 for RM and 0.44 for PS-OSEM. The difference between the two methods was found to be significant at the 1% level. The response of SNR_{ROI} to cut-off frequency is shown in Fig. 5-22. The results indicate that SNR_{ROI} is more dependent on defect contrast than image noise. This is in contrast to the behavior of the CHO, which seems to be heavily dependent on image noise rather than defect contrast.

Reconstruction without the Effects of Attenuation, Scatter, and Detector Response

The reconstructions of the simplified linear projection simulation are shown in Fig. 5-23. In contrast to the results of section 5.3.C, the RM reconstructions appear to have better contrast and uniformity of the activity distribution throughout the LV wall compared to the PS-OSEM images. The findings of this simplified study are in agreement with previous papers [10],[12],[66]. The results suggest that RM may improve upon PS-OSEM in idealized situations, but that these improvements are less dramatic when scatter, attenuation, and detector response are included. Similar results were found in Ch. 3 (Fig. 3-7) which used a physical dynamic phantom that modeled the motion of a beating heart.

Summary and Discussion

In this work we evaluated the detection characteristics of a simultaneous image reconstruction and motion estimation method in terms of lesion detection compared to a standard reconstruction method. A channelized Hotelling observer was used to evaluate reconstructed images from both methods on a central slice in the short-axis view at the end-diastolic frame. The difference in the AUC calculated from the CHO test statistics for the simultaneous and standard methods was not considered to be statistically significant. The methods were further evaluated using a CHO modified for use on gated images. When considering all 8 frames, the difference between the AUC for the simultaneous method and the standard method was not found to be statistically significant.

The SNR of the methods was also evaluated directly using a regions-of-interest method. Using this method it was found that the simultaneous method had a higher SNR_{ROI} than the standard method. The results were found to be significant at the 1% level. There is substantial data relating detectability to SNR [82]-[85] and it may be said that the findings of this ROI SNR investigation show that RM is a better method for lesion detection in cardiac SPECT than the conventional PS-OSEM. However, the results of this study conflict with the results of the CHO studies. We believe that based on the results of *Test 5* and *Test 6* (section 5.3.A and Figs. 5-9 and 5-11) the CHO does not correlate well with the detection characteristics of human observers in the case of varying levels of image smoothness. This is an important finding because it indicates that the CHO cannot be used as a measure of image quality when the methods under investigation have different levels of smoothing. An area of future work will be to further develop and compare the ROI method to human observers.

At least one other author [72] has demonstrated results which conflict with the findings of *Test 5* and *Test 6*. There are several possible reasons for this discrepancy. The phantom

population used in Frey et al. [72] was based on mathematically defined anatomies (ours was based on the Visible Human Project) and the simulation of projection data was carried out using an analytical operator, compared to the Monte Carlo method used here. The defects in [72] were also smaller than in our study, and it may be reasonable to assume that larger defects can lead to higher levels of optimal smoothing using the CHO due to the larger difference in average image intensity. This discrepancy will be the subject of future work.

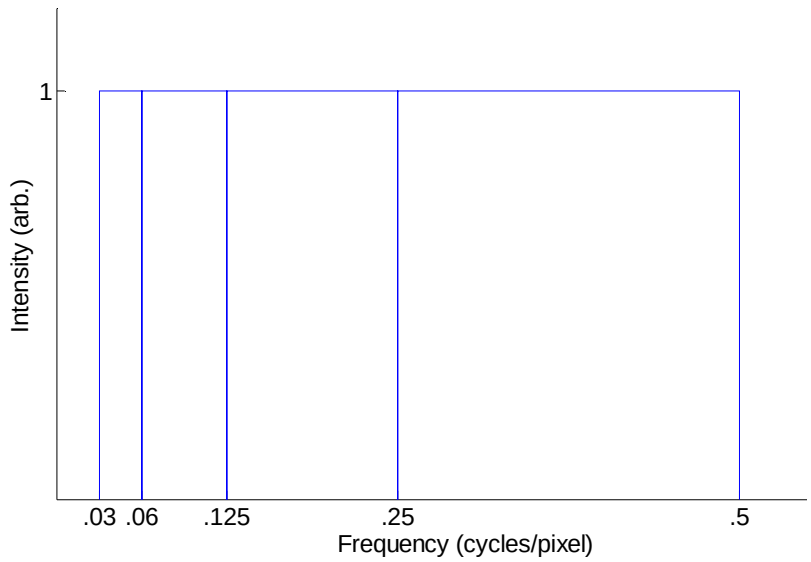

Figure 5-1. Plot of the four frequency bands used in the CHO.

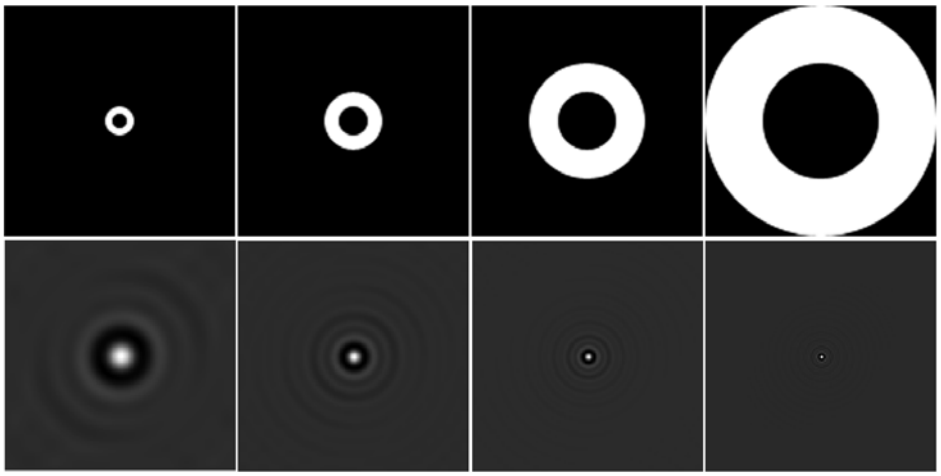

Figure 5-2. The four frequency bands used in the CHO with the zero frequency located at the center of the image (top) and their corresponding spatial domain templates (bottom).

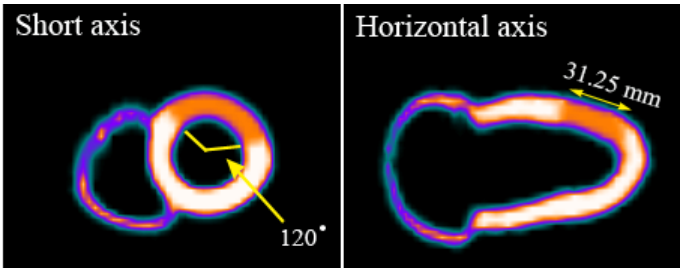

Figure 5-3. Phantom source distributions showing the shape and location of the defect. The images are shown without extra-myocardial activity.

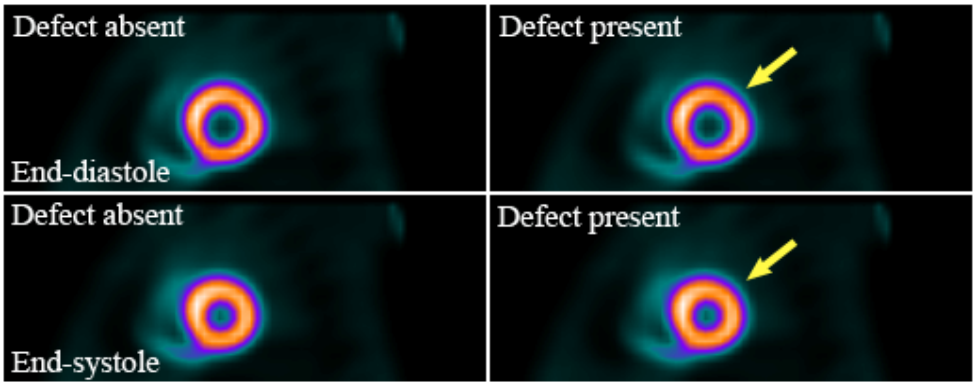

Figure 5-4. Noise-free reconstructions for the normal (left) and abnormal (right) datasets.

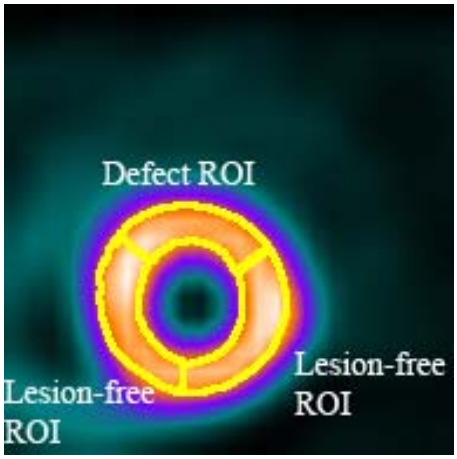

Figure 5-5. ROI's used to calculate SNR directly.

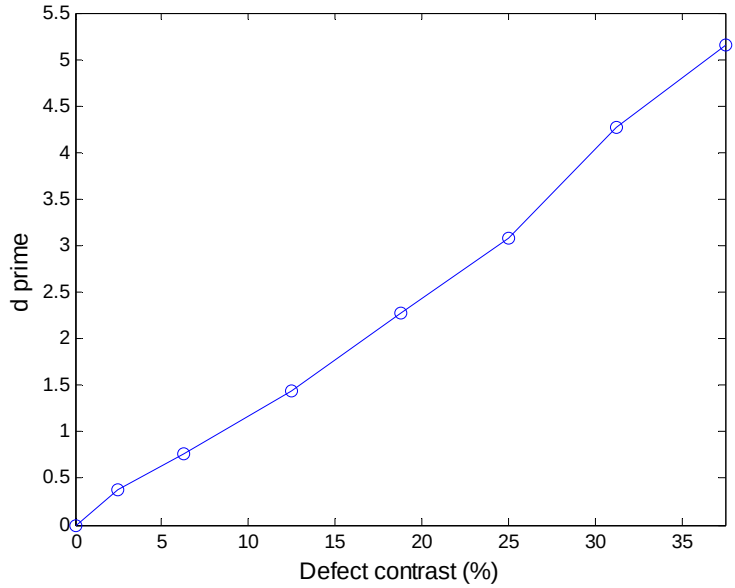

Figure 5-6. d' vs. defect contrast.

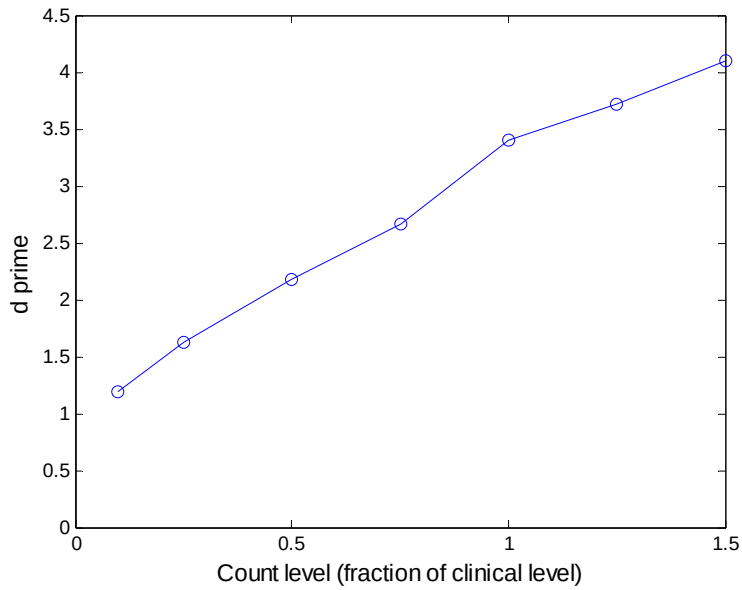

Figure 5-7. d' vs. count level.

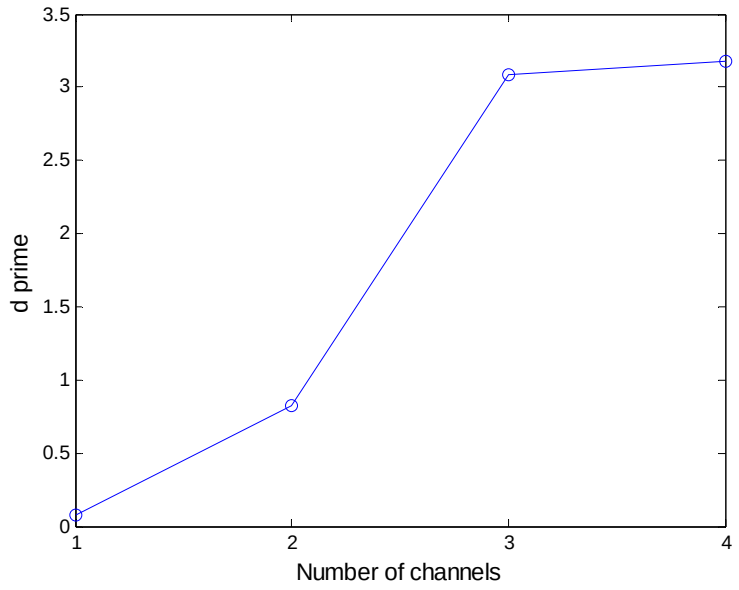

Figure 5-8. d' vs. number of channels used.

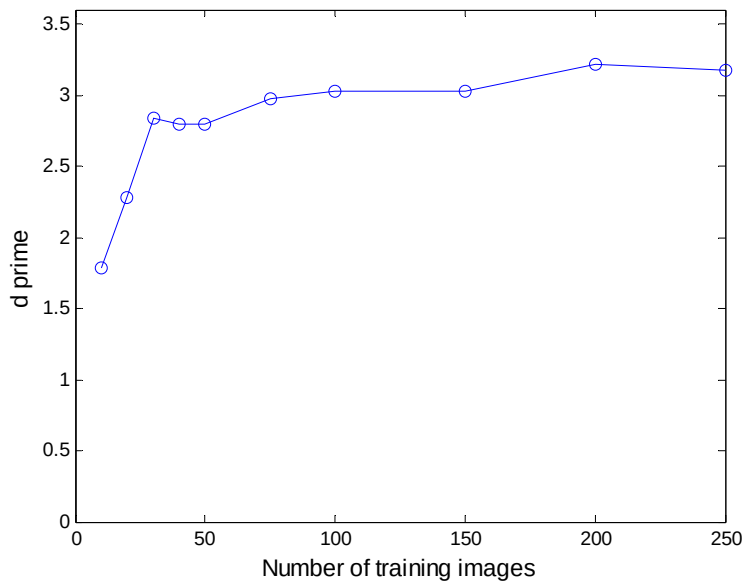

Figure 5-9. d' vs. number of training images used

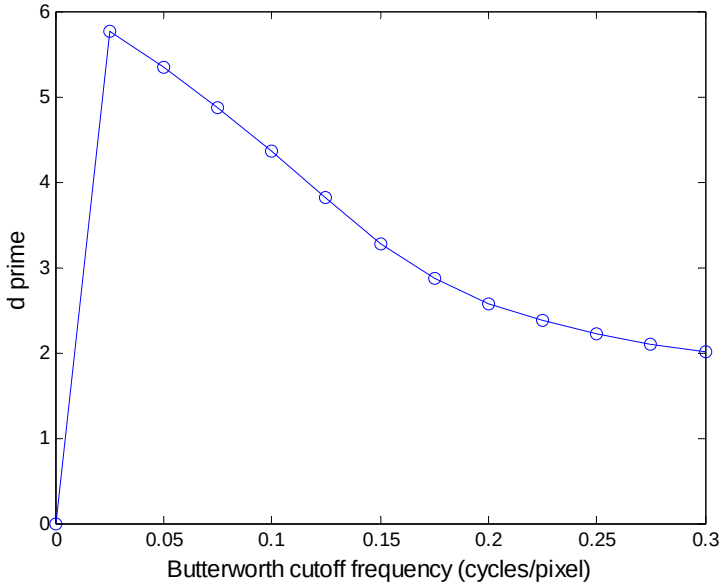

Figure 5-10. d' vs. Butterworth cut-off frequency

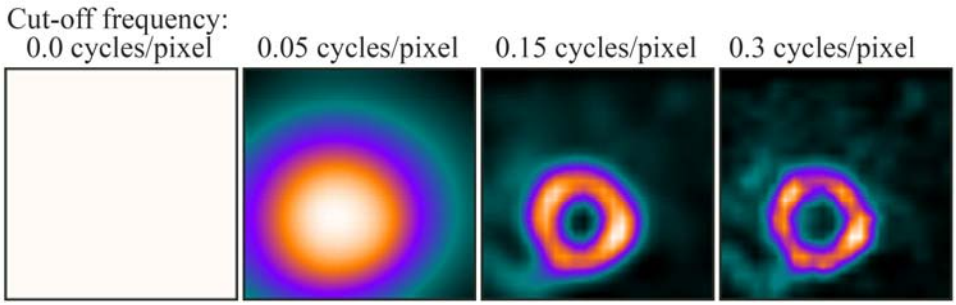

Figure 5-11. Select images used in Figure 5-10.

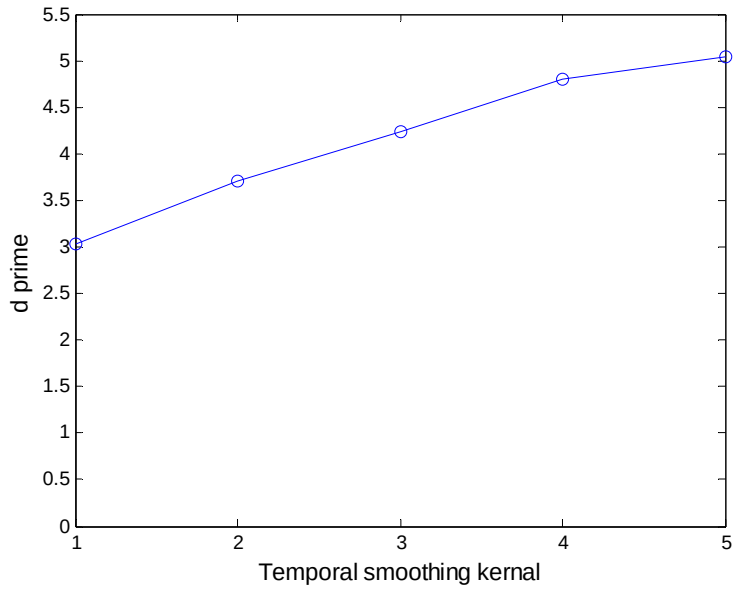

Figure 5-12. d' vs. temporal smoothing kernel number. The weights for each kernel are defined in section 5.2.C.

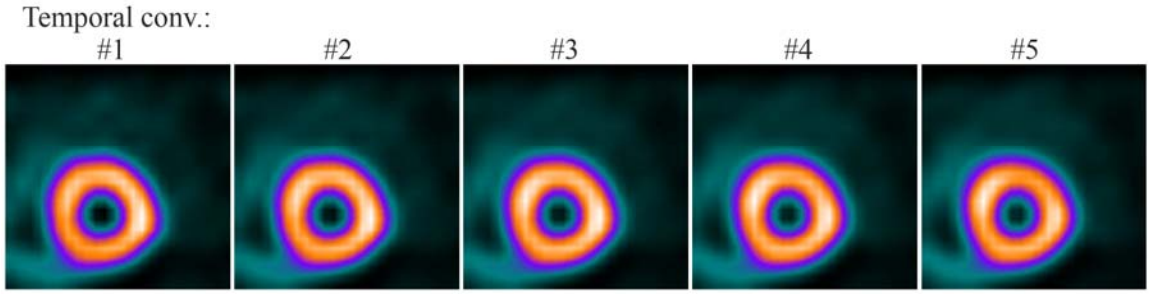

Figure 5-13. Example images of the five levels of temporal smoothing evaluated in Test 6.

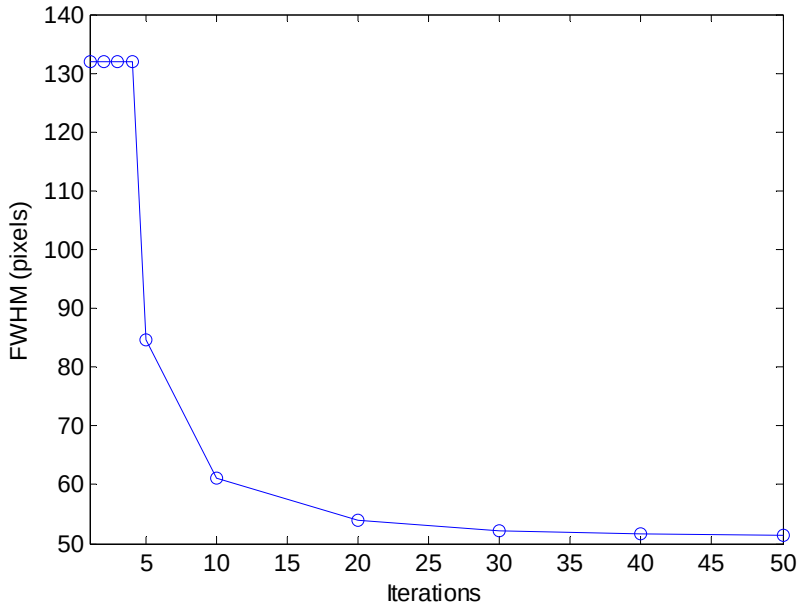

Figure 5-14. FWHM vs MLEM iteration number on noise-free data.

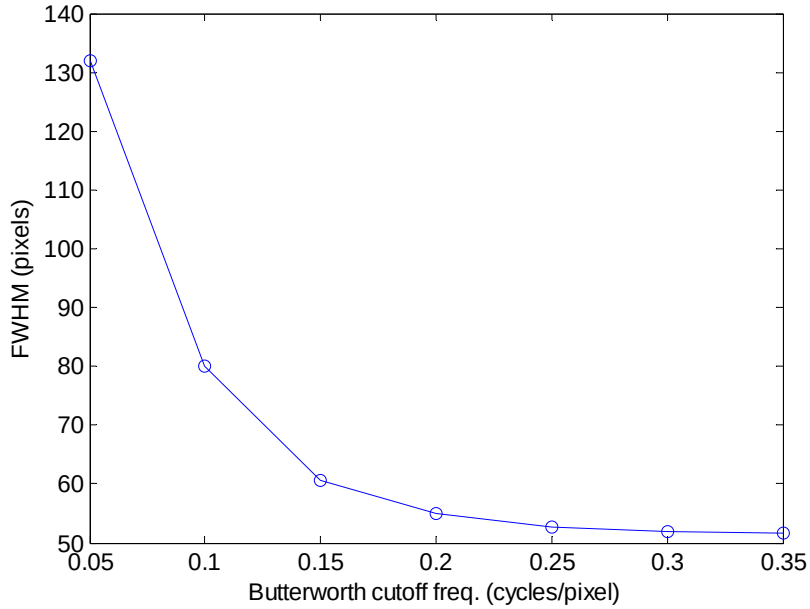

Figure 5-15. FWHM vs Butterworth cut-off frequency on noise-free data.

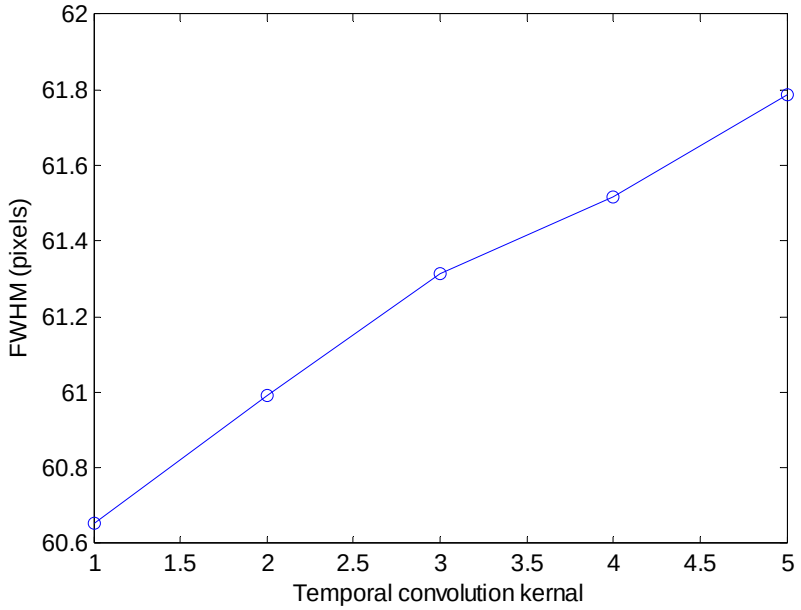

Figure 5-16. The FWHM vs temporal convolution kernal on noise-free data

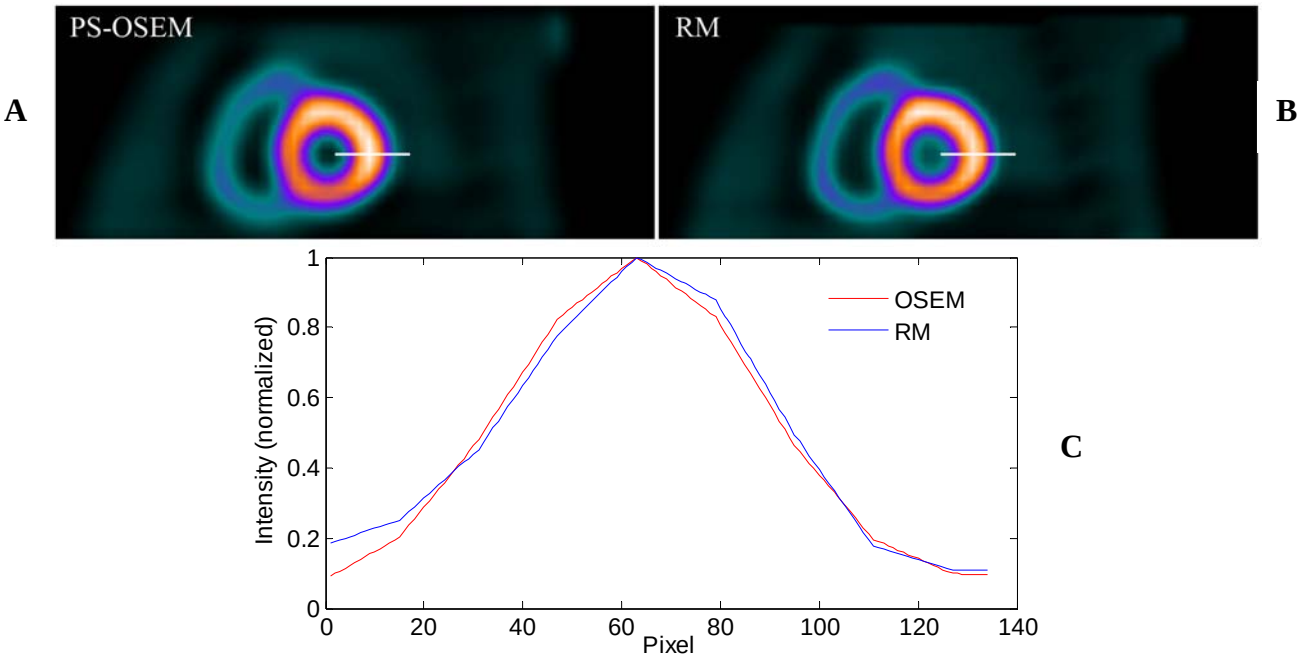

Figure 5-17. Example slices of the A) PS-OSEM and B) RM reconstructed images, and C) their corresponding profiles.

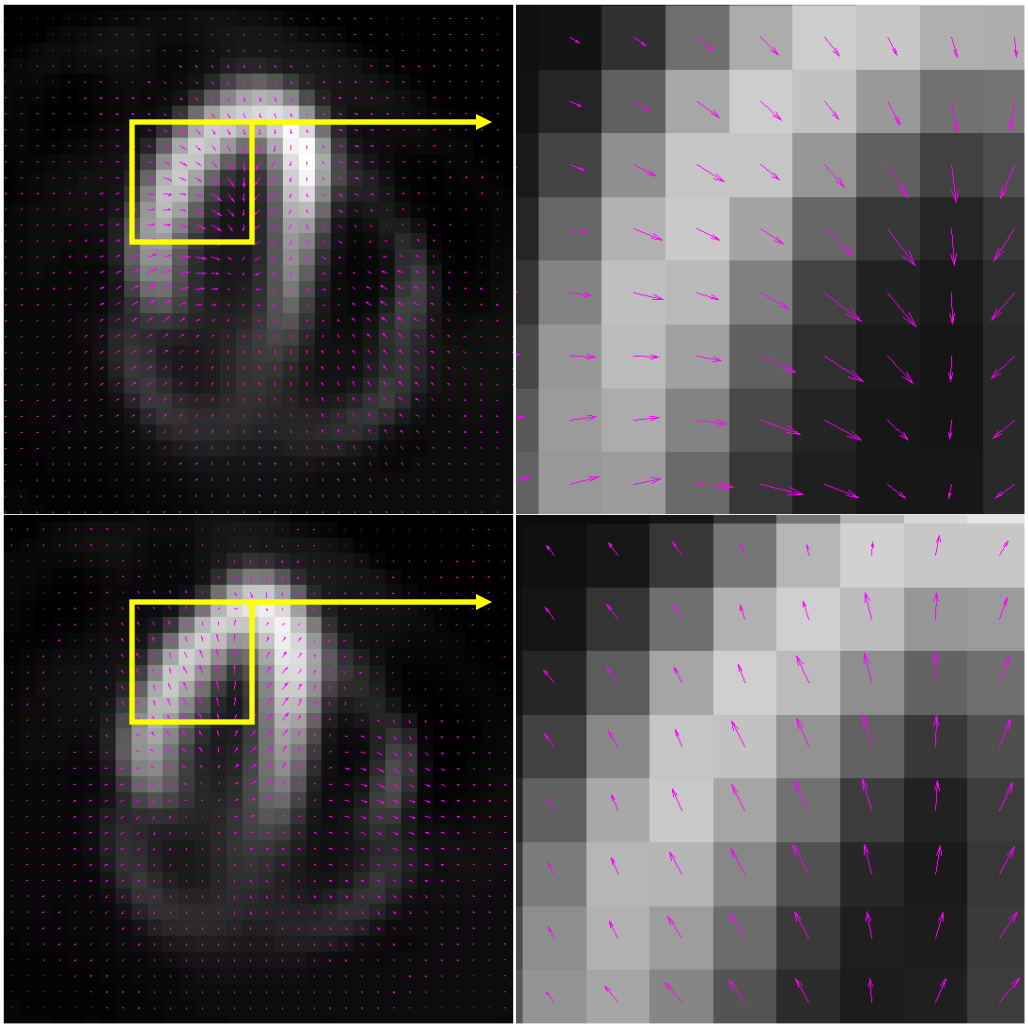

Figure 5-18. Motion vector fields for RM reconstructions in Fig. 5-15 at max-systole (top) and max-diastole (bottom). Areas enclosed with yellow boxes are zoomed in on the right.

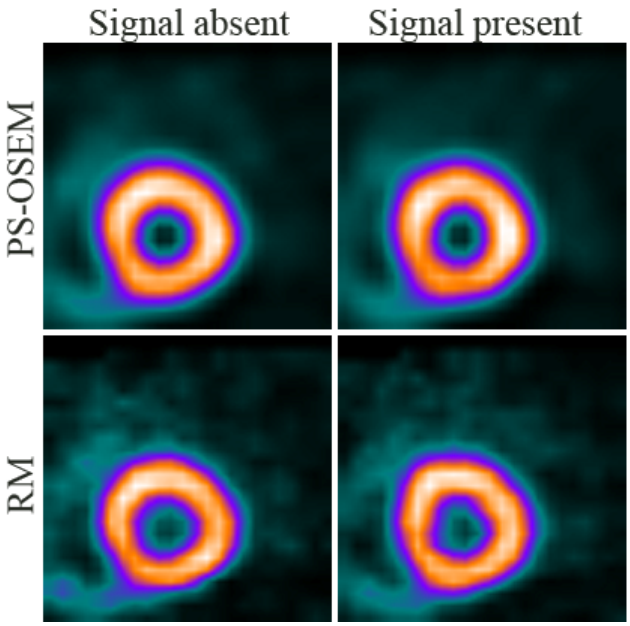

Figure 5-19. Example RM and PS-OSEM images used in the ROC study.

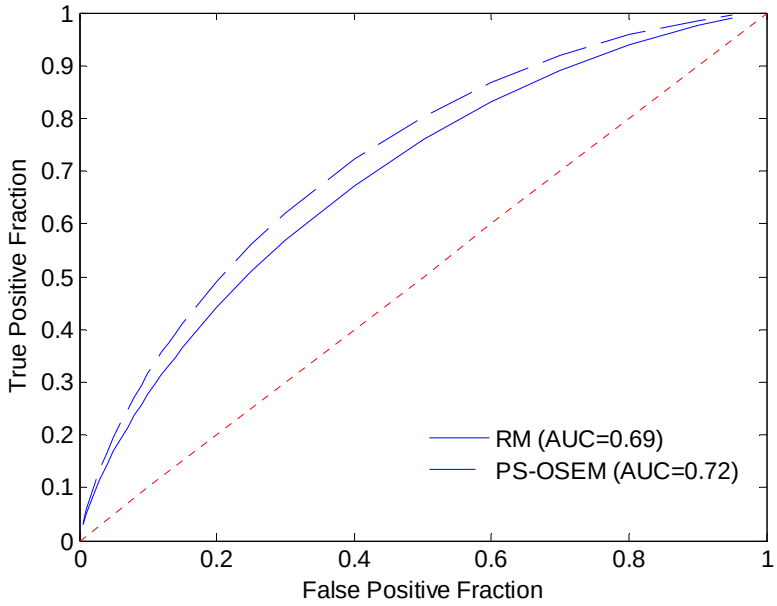

Figure 5-20. ROC curve for RM and PS-OSEM using 2D CHO on a single lesion.

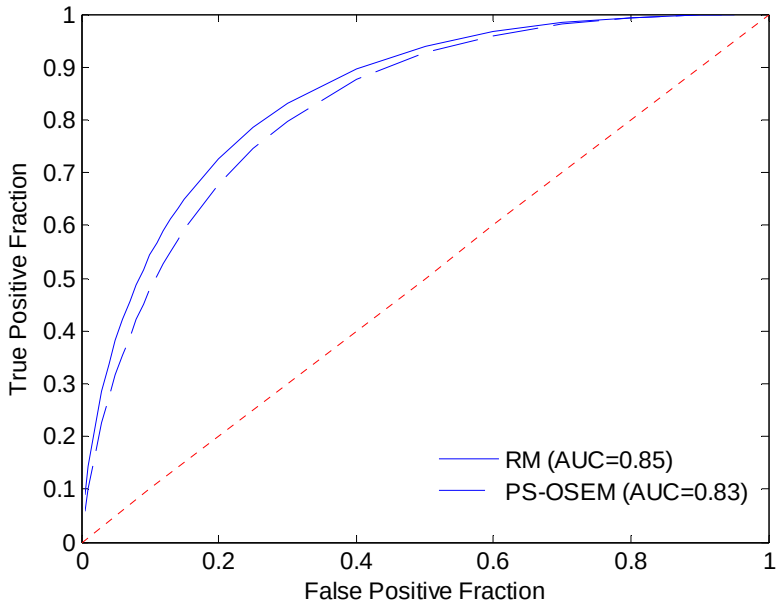

Figure 5-21. ROC curve for RM and PS-OSEM using MACHO on a single lesion.

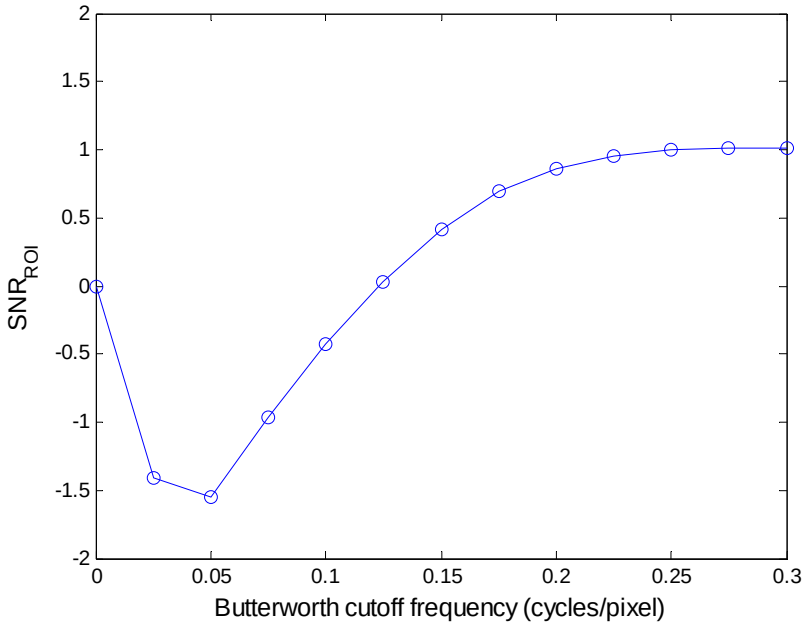

Figure 5-22. SNR_{ROI} vs. 3D Butterworth cut-off frequency.

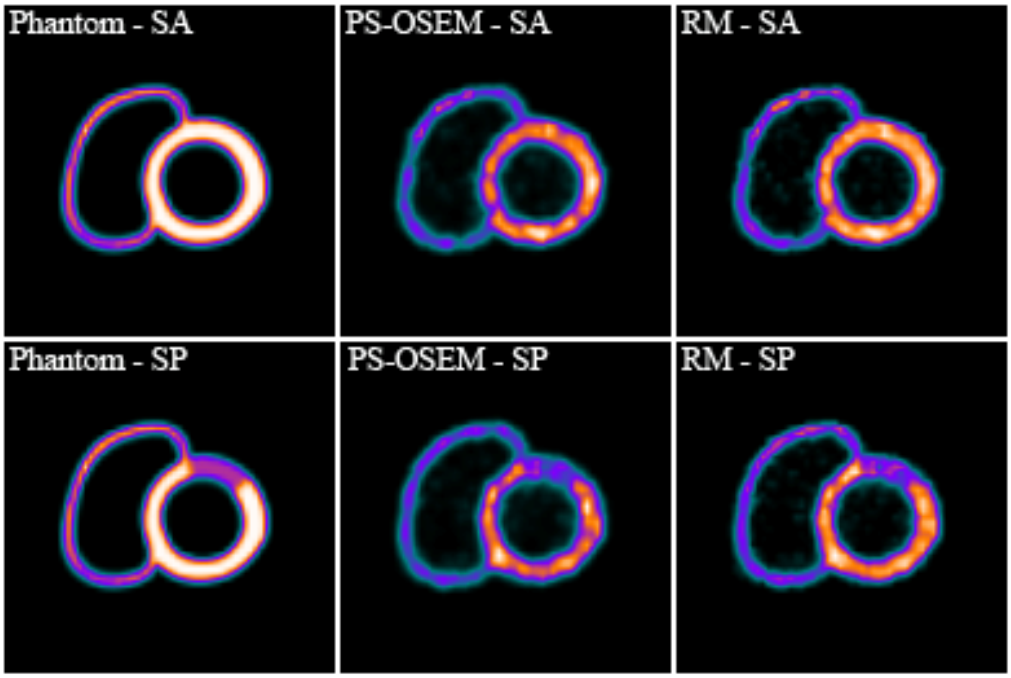

Figure 5-23. Reconstructions of projection data obtained using a simple linear projection operator. RM images appear to have improved contrast and uniformity of the activity distribution throughout the LV wall.

Table 5-1. Relative organ activity concentrations per pixel for the simulated phantom

Organ	Relative activity
Myocardium	75
Heart blood pool	6
Liver	13
Gall bladder	324
Lung	6
Kidney	45
Spleen	45
Bowel	37
Background (body)	6

Table 5-2. Temporal smoothing kernels

Kernel number	Weights	Number of applications
1	{0.0,1.0,0.0}	-
2	{0.1,0.8,0.1}	1
3	{0.1,0.8,0.1}	2
4	{0.25,0.5,0.25}	1
5	{0.33,0.34,0.33}	1

CHAPTER 6
CONCLUSIONS

This dissertation investigated image reconstruction methods incorporating estimated motion in gated imaging. The primary method investigated was a simultaneous image reconstruction and motion estimation approach. In Chapter 3 a physical, dynamic cardiac phantom was modified by attaching point source markers to the phantom epicardial wall. The markers were used to provide an independent measure of the heart wall motion. Acquisitions of the phantom myocardium were reconstructed and the frame-to-frame motion was estimated with the simultaneous method, as well as with a conventional method. It was found that the simultaneous method produced motion estimates with greater motion accuracy than the conventional method. As mentioned in Chapter 3, this study ignored the wringing, or twisting, motion of the heart. A future area of investigation in this area will be an adaptation of the physical phantom to mimic a level of wringing motion found in the human heart. Also, the development of a heart assembly with greater sampling (upwards of 100 marker locations) at both the inner and outer surface of the myocardial chamber will be considered. This will require the development of smaller point source markers to account for the limited space at the inner wall of the phantom myocardium. Also, imaging modalities with greater spatial resolution, such at CT and MR, will be investigated in determining the true marker motion between frames.

In Chapter 4 a new rigid-body motion estimation technique for use in estimating respiration-induced heart motion was developed. The new method used rotation parameterized by a unit quaternion, and the method was compared to several other methods which have been proposed in the literature. The quaternion method was found to be faster, more robust, and more accurate than other techniques across a wide range of reconstructed images. Motion-corrected images using the quaternion method demonstrated improved spatial resolution over uncorrected

images. A future direction of this study will be a receiver operating characteristics analysis comparing the CGQ method with a standard reconstruction method which ignores the effects of respiratory blurring of the heart.

In Chapter 5 the simultaneous image reconstruction and motion estimation method was compared to a standard reconstruction method in clinical practice in terms of lesion detection using a channelized Hotelling observer formulated to operate on single- and multiple-frame reconstructed images. The signal-to-noise ratio of the simultaneous method was also calculated directly using a regions-of-interest method and compared to the standard method. In both the single- and multiple-frame observer studies the differences in detection between the simultaneous method and the standard method were not statistically significant. However, using the regions-of-interest method, the simultaneous method was found to have superior detection properties compared to the standard method. The difference was found to be significant at the 1% level. A future direction of this final study will be an investigation into the discrepancy between the CHO and human observers under varying levels of image smoothness. We will also further investigate the SNR calculation using regions-of-interest as a model of the detection characteristics of human observers.

APPENDIX A
ROTATION MATRIX AND PARTIAL DERIVATIVES

In the Euler representation, Q is the product of the rotation matrices about each axis:

$$\mathrm{Q}(\varphi,\theta,\psi)=\mathrm{Q}_x\mathrm{Q}_y\mathrm{Q}_z=\begin{bmatrix}1 & 0 & 0\\ 0 & \cos\varphi & \sin\varphi\\ 0 & -\sin\varphi & \cos\varphi\end{bmatrix}\begin{bmatrix}\cos\theta & 0 & -\sin\theta\\ 0 & 1 & 0\\ \sin\theta & 0 & \cos\theta\end{bmatrix}\begin{bmatrix}\cos\psi & \sin\psi & 0\\ -\sin\psi & \cos\psi & 0\\ 0 & 0 & 1\end{bmatrix} \tag{A-1}$$

The orthogonal (rotation) matrix Q corresponding to a rotation by (φ,θ,ψ) is:

$$\mathrm{Q}(\varphi,\theta,\psi)=\begin{bmatrix}\cos\theta\cos\psi & \cos\theta\sin\psi & -\sin\theta\\ \sin\varphi\sin\theta\cos\psi-\cos\varphi\sin\psi & \sin\varphi\sin\theta\sin\psi+\cos\varphi\cos\psi & \cos\theta\sin\psi\\ \cos\varphi\sin\theta\cos\psi+\sin\varphi\sin\psi & \cos\varphi\sin\theta\sin\psi-\sin\varphi\cos\psi & \cos\theta\cos\varphi\end{bmatrix} \tag{A-2}$$

In computing the partial derivatives of our objective function, the products $\mathrm{Q}_x\mathrm{Q}_y\mathrm{Q}_z'$, $\mathrm{Q}_x\mathrm{Q}_y'\mathrm{Q}_z$,

and $\mathrm{Q}_x'\mathrm{Q}_y\mathrm{Q}_z$ are needed:

$$\mathrm{Q}_x\mathrm{Q}_y\mathrm{Q}_z'=\begin{bmatrix}-\sin\psi\cos\theta & \cos\psi\cos\theta & 0\\ -\cos\psi\cos\varphi-\sin\psi\sin\varphi\sin\theta & \cos\psi\sin\varphi\sin\theta-\sin\psi\cos\varphi & 0\\ \cos\psi\sin\varphi-\sin\psi\cos\varphi\sin\theta & \cos\psi\cos\varphi\sin\theta+\sin\psi\sin\varphi & 0\end{bmatrix} \tag{A-3}$$

$$\mathrm{Q}_x\mathrm{Q}_y'\mathrm{Q}_z=\begin{bmatrix}-\sin\theta\cos\psi & -\sin\theta\sin\psi & -\cos\theta\\ \cos\theta\cos\psi\sin\varphi & \cos\theta\sin\psi\sin\varphi & -\sin\theta\sin\varphi\\ \cos\theta\cos\psi\cos\varphi & \cos\theta\sin\psi\cos\varphi & -\sin\theta\cos\varphi\end{bmatrix} \tag{A-4}$$

$$\mathrm{Q}_x'\mathrm{Q}_y\mathrm{Q}_z=\begin{bmatrix}0 & 0 & 0\\ \cos\varphi\cos\psi\sin\theta+\sin\varphi\sin\psi & \cos\varphi\sin\psi\sin\theta-\sin\varphi\cos\psi & \cos\psi\cos\theta\\ \cos\varphi\sin\psi-\sin\varphi\cos\psi\sin\theta & -\cos\varphi\cos\psi\sin\theta-\sin\varphi\sin\psi\sin\theta & -\sin\varphi\cos\theta\end{bmatrix} \tag{A-5}$$

APPENDIX B
DETERMINATION OF ROTATION MATRIX

The orthogonal (rotation) matrix R corresponding to a rotation by q is:

$$\mathrm{Q}(\theta_0,\theta_1,\theta_2,\theta_3)=\begin{bmatrix} \theta_0^{\,2}+\theta_1^{\,2}-\theta_2^{\,2}-\theta_3^{\,2} & 2(\theta_1\theta_2-\theta_0\theta_3) & 2(\theta_1\theta_3+\theta_0\theta_2) \\ 2(\theta_1\theta_2+\theta_0\theta_3) & \theta_0^{\,2}-\theta_1^{\,2}+\theta_2^{\,2}-\theta_3^{\,2} & 2(\theta_2\theta_3-\theta_0\theta_1) \\ 2(\theta_1\theta_3-\theta_0\theta_2) & 2(\theta_2\theta_3+\theta_0\theta_1) & \theta_0^{\,2}-\theta_1^{\,2}-\theta_2^{\,2}+\theta_3^{\,2} \end{bmatrix} \tag{B-1}$$

With the substitution $\theta_0 = \sqrt{1-\theta_1^{\,2}-\theta_2^{\,2}-\theta_3^{\,2}}$ in place, the partial derivatives of Q are:

$$\frac{\partial \mathrm{Q}}{\partial \theta_1}=\begin{bmatrix} 0 & 2\left(\theta_2+\frac{\theta_1\theta_3}{\theta_0}\right) & 2\left(\theta_3-\frac{\theta_1\theta_2}{\theta_0}\right) \\ 2\left(\theta_2-\frac{\theta_1\theta_3}{\theta_0}\right) & -4\theta_1 & 2\left(-\theta_3+\frac{\theta_1^{\,2}}{\theta_0}\right) \\ 2\left(\theta_3+\frac{\theta_1\theta_2}{\theta_0}\right) & 2\left(\theta_0-\frac{\theta_1^{\,2}}{\theta_0}\right) & -4\theta_1 \end{bmatrix} \tag{B-2}$$

$$\frac{\partial \mathrm{Q}}{\partial \theta_2}=\begin{bmatrix} -4\theta_2 & 2\left(\theta_1+\frac{\theta_2\theta_3}{\theta_0}\right) & 2\left(\theta_0-\frac{\theta_2^{\,2}}{\theta_0}\right) \\ 2\left(\theta_1-\frac{\theta_2\theta_3}{\theta_0}\right) & 0 & 2\left(\theta_3+\frac{\theta_2\theta_1}{\theta_0}\right) \\ 2\left(-\theta_0+\frac{\theta_2^{\,2}}{\theta_0}\right) & 2\left(\theta_3-\frac{\theta_1\theta_2}{\theta_0}\right) & -4\theta_2 \end{bmatrix} \tag{B-3}$$

$$\frac{\partial \mathrm{Q}}{\partial \theta_3}=\begin{bmatrix} -4\theta_3 & 2\left(-\theta_0+\frac{\theta_3^{\,2}}{\theta_0}\right) & 2\left(\theta_1-\frac{\theta_3\theta_2}{\theta_0}\right) \\ 2\left(\theta_0-\frac{\theta_3^{\,2}}{\theta_0}\right) & -4\theta_3 & 2\left(\theta_2+\frac{\theta_3\theta_1}{\theta_0}\right) \\ 2\left(\theta_1+\frac{\theta_3\theta_2}{\theta_0}\right) & 2\left(\theta_2-\frac{\theta_3\theta_1}{\theta_0}\right) & 0 \end{bmatrix} \tag{B-4}$$

APPENDIX C
PARTIAL DERIVATIVES USED IN CGQ ALGORITHM

The partial derivatives of E with respect to each of the parameters are:

$$\frac{\partial E(\mathrm{Q},\mathbf{b})}{\partial \theta_1} = -2\sum_{\mathbf{r}}\left(f_1(\mathbf{r}) - f_j(\mathrm{Q}\mathbf{r}+\mathbf{b})\right)\nabla f_j\left(\mathrm{Q}\mathbf{r}+\mathbf{b}\right)\frac{\partial \mathrm{Q}}{\partial \theta_1}\mathbf{r} \tag{C-1}$$

$$\frac{\partial E(\mathrm{Q},\mathbf{b})}{\partial \theta_2} = -2\sum_{\mathbf{r}}\left(f_1(\mathbf{r}) - f_j(\mathrm{Q}\mathbf{r}+\mathbf{b})\right)\nabla f_j\left(\mathrm{Q}\mathbf{r}+\mathbf{b}\right)\frac{\partial \mathrm{Q}}{\partial \theta_2}\mathbf{r} \tag{C-2}$$

$$\frac{\partial E(\mathrm{Q},\mathbf{b})}{\partial \theta_3} = -2\sum_{\mathbf{r}}\left(f_1(\mathbf{r}) - f_j(\mathrm{Q}\mathbf{r}+\mathbf{b})\right)\nabla f_j\left(\mathrm{Q}\mathbf{r}+\mathbf{b}\right)\frac{\partial \mathrm{Q}}{\partial \theta_3}\mathbf{r} \tag{C-3}$$

$$\frac{\partial E(\mathrm{Q},\mathbf{b})}{\partial b_x} = -2\sum_{\mathbf{r}}\left(f_1(\mathbf{r}) - f_j(\mathrm{Q}\mathbf{r}+\mathbf{b})\right)\frac{\partial f_j(\mathrm{Q}\mathbf{r}+\mathbf{b})}{\partial x} \tag{C-4}$$

$$\frac{\partial E(\mathrm{Q},\mathbf{b})}{\partial b_y} = -2\sum_{\mathbf{r}}\left(f_1(\mathbf{r}) - f_j(\mathrm{Q}\mathbf{r}+\mathbf{b})\right)\frac{\partial f_j(\mathrm{Q}\mathbf{r}+\mathbf{b})}{\partial y} \tag{C-5}$$

$$\frac{\partial E(\mathrm{Q},\mathbf{b})}{\partial b_z} = -2\sum_{\mathbf{r}}\left(f_1(\mathbf{r}) - f_j(\mathrm{Q}\mathbf{r}+\mathbf{b})\right)\frac{\partial f_j(\mathrm{Q}\mathbf{r}+\mathbf{b})}{\partial z} \tag{C-6}$$

REFERENCES

[1] A.M. Minino, M.P. Heron, S.L. Murphy, and K.D. Kochankek, "Deaths: final data for 2004. National vital statistics reports," *National Center for Health Statistics,* vol. 55, no. 19, 2007.

[2] C.Y. Loong and C. Anagnostopoulos, "Diagnosis of coronary artery disease by radionuclide myocardial perfusion imaging," *Heart*, vol. 90, pp. 2-9, 2004.

[3] A.F. Schinkel, J.J. Bax, A. Elhendy, et al., "Long-term prognostic value of dobutamine stress echocardiography compared with myocardial perfusion scanning in patients unable to perform exercise tests," *Am. J. Med.,* vol. 117, pp. 1-9, 2004.

[4] T. Marwick, B. Willemart, A.M. D'Hondt, et al., "Selection of the optimal nonexercise stress for the evaluation of ischemic regional myocardial dysfunction and malperfusion. Comparison of dobutamine and adenosine using echocardiography and ^{99m}Tc-MIBI sinlge photon emission computed tomography," *Circulation*, vol. 87, pp. 345-354, 1993.

[5] R.D. Des Prez, L.J. Shaw, R.L. Gillespie, W.A. Jaber, G.L. Noble, P. Soman, D.G. Wolinsky, and K.A. Williams, "Cost-effectiveness of myocardial perfusion imaging: A summary of the currently available literature," *J. Nucl. Cardiol.,* vol. 12, pp. 750-759, 2005.

[6] B.H. Duncan, A.W. Ahlberg, M.G. Levine, et al., "Comparison of electrocardiographic gated technetium-99m sestimibi single-photon emission computed tomographic imaging and rest-redistribution thallium-201 in the prediction of myocardial viability," *Am. J. Cardiology*, vol. 85, pp. 680-684, 2000.

[7] T.M. Bateman, D.S. Berman, G.V. Heller, et al., "American Society of Nuclear Cardiology position statement on electrocardiographic gating of myocardial perfusion SPECT scintigrams," *J. Nucl. Cardiol.*, vol. 6, pp. 470-471, 1999.

[8] D.S. Lalush and B.M.W. Tsui, "Simulation evaluation of Gibbs prior distributions for use in maximum *a posteriori* SPECT reconstructions," *Trans. Med. Imag.*, vol. 11, pp. 267-275, 1990.

[9] D.S. Lalush, L. Cui, and B.M.W. Tsui, "*A priori* models for four-dimensional reconstruction in gated cardiac SPECT," *Nuc. Sci. Symp. Conf. Rec.*, vol. 3, pp. 1923-1927, 1996.

[10] D.R. Gilland, B.A. Mair, J.E. Bowsher, and R.J. Jaszczak, "Simultaneous reconstruction and motion estimation for gated cardiac ECT," *IEEE Trans. Nucl. Sci.,* vol. 49, no. 5, pp. 2344-2349, 2002.

[11] L.A. Shepp and Y. Vardi, "Maximum likelihood reconstruction for emission tomography," *IEEE Trans. Med. Img.*, vol. MI-1, no. 2, pp. 113-122, 1982.

[12] B.A. Mair, D.R. Gilland, and J. Sun, "Estimation of images and nonrigid deformations in gated emission CT," *IEEE Trans. Med. Imag.*, vol. 25, no. 9, pp. 1130-1144, 2006.

[13] H. Hudson and R. Larkin, "Accelerated image reconstruction using ordered-subsets of projection data," *IEEE Trans. Med. Imag.*, v. 13, no. 4, pp. 601-609, 1994.

[14] M.M. Ter-Pogossian, S.R. Bergmann, and B.E. Sobel, "Influence of cardiac and respiratory motion on tomographic reconstructions of the heart: implications for quantitative nuclear cardiology," *J. Comp. Asst. Tomo.*, vol. 6, pp. 1148-1155, 1982.

[15] Y. Wang, S.J. Riederer, and R.L. Ehman, "Respiratory motion of the heart: Kinematics and the implications for the spatial resolution in coronary imaging," *Magn. Reson. Med.*, vol. 33, pp. 713-719, 1995.

[16] K. McLeish, D.L.G. Hill, D. Atkinson, J.M. Blackall, and R. Razavi, "A study of the motion and deformation of the heart due to respiration," *IEEE Trans. Med. Img.,* vol. 21, no. 9, pp. 1142-1150, 2002.

[17] P.P. Bruyant, M.A. Gennert, G.C. Speckert, R.D. Beach, J.D. Morgenstern, N. Kumar, S. Nadella, and M.A. King, "A robust visual tracking system for patient motion detection in SPECT: Hardware solutions," *IEEE Trans. Nucl. Sci.*, vol. 52, pp. 1288-1294, 2005.

[18] G. Kovalski, O. Israel, Z. Keidar, A. Frenkel, J. Sachs, and H. Azhari, "Correction of heart motion due to respiration in clinical myocardial perfusion SPECT scans using respiratory gating," *J. Nuc. Med.,* vol. 48, no. 4, 630-636, 2007.

[19] R.D. Fiete, H.H. Barrett, W.E. Smith, and K.J. Myers, "Hotelling trace criterion and its correlation with human-observer performance," *J. Opt. Soc. Am. A.,* vol. 4, no. 5, pp. 945-953, 1987.

[20] C.E. Metz, "Basic principles of ROC analysis," *Seminars in Nucl Med.,* vol. 8, pp. 283-298, 1978.

[21] J. Yao, and H.H. Barrett, "Predicting human performance by a channelized Hotelling observer model," *Mathematical Methods in Medical Imaging, SPIE,* vol. 1768, pp. 161-168, 1992.

[22] R.L. DeValois and K.K. DeValois, "Spatial vision," Oxford University press, New York, 1988.

[23] D.S. Lalush and B.M.W. Tsui, "Block iterative techniques for fast 4D reconstruction using a priori motion models in gated cardiac SPECT," *Phys. Med. Biol.,* vol. 43, no. 4, pp. 875–886, 1998.

[24] E. Gravier and Y. Yang, "Motion-compensated reconstruction of tomographic image sequences," *IEEE Nuclear Science Symposium Conference Record*., vol 4, pp. 2927–2931, 2003.

[25] S.M. Song and R.M. Leahy, "Computation of 3–D velocity fields from 3–D cine CT images of a human heart," *IEEE Trans. Med. Imag.*, vol. 10, pp. 295–306, 1991.

[26] G.J. Klein, B.W. Reutter, and R.H. Huesman, "Non–rigid summing of gated PET via optical flow," *IEEE Trans. Nucl. Sci.*, vol. 44, no. 4, pp. 1509–1512, 1997.

[27] G.J. Klein and R.H. Huesman, "Elastic material model mismatch effects in deformable motion estimation," *IEEE Trans. Nucl. Sci.*, vol. 47, no. 3, pp. 1000–1005, 2000.

[28] G.J. Klein and R.H. Huesman, "Four-dimensional processing of deformable cardiac PET data," *Medical Image Analysis*, vol. 6, pp. 29–46, 2002.

[29] B.K. Horn and B.G. Schunck, "Determining optical flow," *Artif. Intell.*, vol. 17, pp. 185-203, 1981.

[30] H.M. Hudson and P. Larkin, "Accelerated EM reconstruction using ordered subsets," *Trans. Med. Img.,* vol. 13, no. 4, pp. 601-609, 1994.

[31] A.A. Young and L. Axel, "Three-dimensional motion and deformation of the heart wall: Estimation with spatial modulation of magnetization – a model-based approach," *Radiology*, vol. 185, pp. 241-247, 1992.

[32] A. Mitiche and P. Bourthemy, "Computation and analysis of image motion: A synopsis of current problems and methods," *Int. J. Comput. Vision*, vol. 19, no. 1, pp. 29-55, 1996.

[33] L. Livieratos, K. Rajappan, L. Stegger, K. Schafers, D.L. Bailey, P.G. Camici, "Respiratory gating of cardiac PET data in list-mode acquisition," *Eur. J. Nucl. Med.,* vol. 33, no. 5, pp. 584-588, 2006.

[34] G. Shechter, C. Ozturk, J.R. Resar, E.R. McVeigh, "Respiratory motion of the heart from free breathing coronary angiograms," *IEEE Trans Med Imag.,* vol. 23, no. 8, pp. 1046–1056, 2004.

[35] G.J. Klein, B.W. Reutter, M.H. Hol, J.H. Reed, R.H. Huesman, "Real-time system for respiratory-cardiac gating in positron tomography," *IEEE Trans Nucl Sci.,* vol. 45, no. 4, pp. 2139–2143, 1998.

[36] A. Martinez-Moller, D. Zikic, R.M. Botnar, R.A. Bundschuh, W. Howe, S.I. Ziegler, N. Navab, M. Schwaiger, S.G. Nekolla, "Dual cardiac–respiratory gated PET: implementation and results from a feasibility study," *Eur. J. Nuc. Med. Mol. Img*., vol. 34, no. 9, pp. 1447-1154, 2007.

[37] E.J. Hoffman, M.E. Phelps, G. Wisenberg, H.R. Schelbert, D.E. Kuhl, "Electrocardiographic gating in positron emission computed tomography," *J. Comput. Assist. Tomogr.,* vol. 3, pp. 733-739, 1979.

[38] N.C. Detorie, A.L. Kesner, T.D. Solberg, M. Dahlbom, "Evaluation of image noise in respiratory gated PET," *IEEE Trans. Nuc. Sci.,* vol. 54, no. 1, pp. 66-70, 2007.

[39] R.D. Beach, P.H. Pretorius, G. Boening, P.P. Bruyant, B. Feng, R.R. Fulton, M.A. Gennert, S. Nadella, and M.A. King, "Feasibility of stereo-infrared tracking to monitor patient motion during cardiac SPECT imaging," *IEEE Trans. Nucl. Sci.*, vol. 51, no. 5, pp. 2693–2698, 2004.

[40] R.D. Beach, H. Depold, G. Boening, P.P. Bruyant, B. Feng, H.C. Gifford, M.A. Gennert, S. Nadella, M.A. King, "An adaptive approach to decomposing patient-motion tracking data acquired during cardiac SPECT imaging," *IEEE Trans. Nuc. Sci.* vol. 54, no. 1, pp. 130-139, 2007.

[41] P.P. Bruyant, M.A. King, P.H. Pretorius, "Correction of the respiratory motion of the heart by tracking of the center of mass of thresholded projections: A simulation study using the dynamic MCAT phantom," *IEEE Trans. Nucl. Sci.,* vol. 49, no. 5, pp. 2159-2166, 2002.

[42] B. Feng, P.P. Bruyant, P.H. Pretorius, R.D. Beach, H.C. Gifford, J. Dey, M.A. Gennert, M.A. King, "Estimation of the rigid-body motion from three-dimensional images using a generalized center-of-mass points approach," *IEEE Trans. Nucl. Sci.*, vol. 53, no. 5, pp. 2712-2718, 2006.

[43] L. Livieratos, L. Stegger, P.M. Bloomfield, K. Schafers, D.L. Bailey, P.G. Camici, "Rigid-body transformation of list-mode projection data for respiratory motion correction in cardiac PET," *Phys. Med. Biol.*, vol. 50, pp. 3313-3322, 2005.

[44] G.J. Klein, B.W. Reutter, R.H. Huesman, "Four-dimensional affine registration models for respiratory-gated PET," *IEEE Trans. Nucl. Sci.,* vol. 48, no. 3, pp. 756-760, 2001.

[45] J. Dey, B. Feng, K.L. Johnson, J.E. McNamara, P.H. Pretorius, M.A. King, "Respiratory motion correction in cardiac SPECT using affine and free-form deformation registration with temporal and spatial constraints," *Proc. 9th Int. Meeting Fully3D Image Rec. Rad. Nucl. Med.,* pp. 201-204, 2007.

[46] J.G. Parker, B.A. Mair, D.R. Gilland, M. Mahoney, "Cardiac emission tomography with 3D respiratory motion correction," *Proc. 9th Int. Meeting Fully3D Image Rec. Rad. Nucl. Med.,* pp. 413-416, 2007.

[47] W. Lu, P.J. Parikh, J.P. Hubenschmidt, J.D. Bradley, D.A. Low, "A comparison between amplitude sorting and phase-angle sorting using external respiratory measurement for 4D CT," *Med. Phys.,* vol. 33, no. 8, pp. 2964-2974, 2006.

[48] H.W. Korin, R.L. Ehman, S.J. Riederer, J.P. Felmlee, R.C. Grimm, "Respiratory kinematics of the upper abdominal organs: a quantitative study," *Magn Reson. Med.,* vol. 23, pp. 172-178, 1992.

[49] P. Thevenaz, U.E. Ruttimann, M. Unser, "A pyramid approach to subpixel registration based on intensity," *IEEE Trans. Image Proc.,* vol. 7, no. 1, pp. 27-41, 1998.

[50] V. Kantabutra, "On hardware for computing exponential and trigonometric functions," *IEEE Trans. Comp.*, vol. 45, no. 3, pp. 328-39, 1996.

[51] B.K.P. Horn, “Closed-form solution of absolute orientation using unit quaternions,” *J. Opt. Soc. of America A.*, vol. 4, pp. 629-642, 1987.

[52] R. Mukundan, “Quaternions: From classical mechanics to computer graphics, and beyond,” *Proc. 7th Asian Tech. Conf. in Mathematics.* Invited paper. Melaka, Malaysia, Dec. 18-21, 2002.

[53] W.W. Hagar and H. Zhang, “A new conjugate gradient method with guaranteed descent and an efficient line search,” *SIAM J. Optimization.* vol. 16, pp. 170-192, 2005.

[54] W.W. Hagar and H. Zhang, “Algorithm 851: CG_DESCENT, A conjugate gradient method with guaranteed descent,” *ACM Trans. Math. Soft.* vol. 32, pp. 113-137, 2006.

[55] T.L. Faber and E.M. Stokely, “Orientation of 3-D structures in medical images,” *IEEE Trans. Pattern Anal. and Mach. Intel.,* vol. 10, no. 5, pp. 626-633, 1988.

[56] N.M. Alpert, J.F. Bradshaw, D. Kennedy, J.A. Correia, “The principal axes transformation – A method for image registration,” *J. Nucl. Med.* vol. 31, pp. 1717-1722, 1990.

[57] E. Anderson, Z. Bai, C. Bischof, S. Blackford, J. Demmel, J. Dongarra, J. Du Croz, A. Greenbaum, S. Hammarling, A. McKenney, D. Sorensen, LAPACK Users’ Guide Third Edition, Knoxville, University of Tennessee, 1999.

[58] W.H. Press, B.P. Flannery, S.A. Teukolsky, W.T. Vetterling, Numerical Recipes in C: The Art of Scientific Computing, Cambridge University Press, 1993.

[59] W.P. Segars, D.S. Lalush, B.M.W. Tsui, "A Realistic spline-based dynamic heart phantom," *IEEE Trans. Nucl. Sci.* vol. 46, no. 3, pp. 503-506, 1999.

[60] D.R. Gilland, R.J. Jaszczak, M.W. Hanson, K.L. Greer, R.E. Coleman, “An experimental phantom based on quantitative SPECT analysis of patient MIBI biodistribution,” *J. Nucl. Med.,* vol. 37, no. 154P, 1996.

[61] M. Ljungberg and S.E. Strand, “A Monte-Carlo program simulating scintillation camera imaging,” *Comp. Meth. Progr. Biomed.* vol. 29, pp. 257-272, 1989.

[62] K.J. Myers and H.H. Barrett, “Addition of a channel mechanism to the ideal-observer model,” *J. Opt. Soc. Amer.,* vol. 4, pp. 2447-2457, 1987.

[63] M. Chen, J.E. Bowsher, A.H. Baydush, K.L. Gilland, D.M. DeLong, R.J. Jaszczak, “Using the Hotelling observer on multislice and multiview simulated SPECT myocardial images,” *IEEE Trans. Nuc. Sci.*, vol. 49, no. 3, pp. 661-667, 2002.

[64] Z. Cao, D.R. Gilland, B.A Mair, B.M.W. Tsui, “An observer model evaluation of simultaneous reconstruction and motion estimation for emission tomography,” *IEEE Int. Symp. Biomed. Img.: Nano to Macro.,* vol. 1, pp. 940-943, 2004.

[65] E. Gravier, Y. Yang, M.A. King, and M. Jin, "Fully 4D motion-compensated reconstruction of cardiac SPECT images," *Phys. Med. Bio.,* vol. 51, pp. 4603-4619, 2006.

[66] Z. Cao, D.R. Gilland, B.A. Mair, R.J. Jaszczak, "Three-dimensional motion estimation with image reconstruction for gated cardiac ECT," *IEEE Trans. Nuc. Sci.,* vol. 50, no. 3, pp. 384-388, 2003.

[67] J.G. Parker, D.R. Gilland, "Wall motion estimation for gated cardiac emission tomography: physical phantom evaluation," *IEEE Trans. Nuc. Sci.,* vol. 55, no. 1, pp. 531-536, 2008.

[68] H.H. Barrett, J. Yao, J.P. Rolland, K.J. Myers, "Model observers for assessment of image quality," *Proc. Nat. Acad. Sci. USA*, vol., 90, pp. 9758-9765, 1993.

[69] H.C. Gifford, M.A. King, D.J. de Vries, E.J. Soares, "Channelized Hotelling and human observer correlation for lesion detection in hepatic SPECT imaging," *J. Nuc. Med.,* vol. 41, pp. 514-521, 2000.

[70] K.J. LaCroix, B.M.W. Tsui, E.C. Frey, "Rotationally symmetric vs. oriented frequency channels for the Hotelling observer: A comparison with human observers," *IEEE Nuc. Sci. Symp. Conf. Rec.,* vol. 3, pp. 1402-1406, 1999.

[71] S.D. Wollenweber, B.M.W. Tsui, D.S. Lalush, E.C. Frey, K.J. LaCroix, G.T. Gullberg, "Comparison of Hotelling observer models and human observers in defect detection from myocardial SPECT imaging," *IEEE Trans. Nuc. Sci.,* vol. 46, no. 6, pp. 2098-2103, 1999.

[72] E.C. Frey, K.L. Gilland, B.M.W. Tsui, "Application of Task-Based Measures of Image Quality to Optimization and Evaluation of Three-Dimensional Reconstruction-Based Compensation Methods in Myocardial Perfusion SPECT," *IEEE Trans. Med. Img.,* vol. 21, no. 9, pp. 1040-1050, 2002.

[73] D.R. Gilland, B.M.W. Tsui, W.H. McCartney, J.R. Perry, J. Berg, "Determination of the Optimum Filter Function for SPECT Imaging," *J. Nuc. Med.,* vol. 29, pp. 643-650, 1988.

[74] P. Green, "Bayesian reconstructions from emission tomography using a modified EM algorithm," *IEEE Trans. Med. Img.,* vol. 9, no. 1, pp. 84-93, 1990.

[75] D.R. Gilland, B.A. Mair, J.G. Parker, "Motion estimation for cardiac emission tomography by optical flow methods," *Phys. Med. Bio.,* vol. 53, pp. 2991-3006, 2008.

[76] M. Chen, R.J. Jaszczak, J.E. Bowsher, D.R. Gilland, "An evaluation of cardiac uniformity, contrast, and SNR with dual-head 180° and triple-head 360° SPECT scans," *IEEE Trans. Nuc. Sci.,* vol. 48, no. 4, pp. 1428-1434, 2001.

[77] S.D. Wollenweber, B.M.W. Tsui, D.S. Lalush, E.C. Frey, G.T. Gullberg, "Evaluation of myocardial defect detection between parallel-hole and fan-beam SPECT using the Hotelling trace," *IEEE Nuc. Sci. Symp. Conf. Rec.* vol. 2, pp. 1428-1432, 1998.

[78] C.K. Abbey, H.H. Barrett, M.P. Eckstein, "Practical issues and methodology in assesment of image quality using model observers," *SPIE Med. Img. Symp.,* vol. 3032, pp. 182-194, 1997.

[79] K. Fukunaga, R.R. Hayes, "Effects of sample size in classifier design," *IEEE Trans. Pattern Analysis Mach. Int.,* vol. 11, pp. 873-885, 1989.

[80] R.F. Wagner, H.P. Chan, B. Sahiner, N. Petrick, J.T. Mossoba, "Finite-sample effects and resampling plans: Applications to linear classifiers in computer-aided diagnosis," *SPIE Img. Proc. Conf.,* vol. 3034, pp. 467-477, 1997.

[81] M.V. Narayanan, H.C. Gifford, M.A. King, P.H. Pretorius, T.H. Farncombe, P. Bruyant, M.N. Wernick, "Optimization of Iterative Reconstructions of ^{99m}Tc Cardiac SPECT Studies Using Numerical Observers," *IEEE Trans. Nuc. Sci.* vol. 49, no. 5, pp. 2355-2360, 2002.

[82] H. Devries, "The quantum character of light and its bearing upon threshold of vision, the differential sensitivity and visual acuity of the eye," *Physica* (*Utrecht*), vol. 10, pp. 553-564, 1943.

[83] A. Rose, "The sensitivity performance of the human eye on an absolute scale," *J. Opt. Soc. Am.,* vol. 38, pp. 196-208, 1948.

[84] A. Rose, "Television pickup tubes and the problem of vision," *Adv. Electron.,* vol. 1, p. 131, 1948.

[85] L.M. Biberman, ed., "Perception of displayed information," Plenum, New York, 1973.

BIOGRAPHICAL SKETCH

Jason Glenn Parker was born on October 26, 1979, in Orlando, FL. He was the oldest of four children and grew up in Venice, FL. He earned an A.A. at Manatee Community College in 2002, a B.S. at Rensselaer Polytechnic Institute in 2005, and a Ph.D. from the University of Florida in 2008. After graduating from UF he will begin working as a Senior Scientist in Dayton, OH, supervising research into advanced magnetic resonance imaging techniques.